SPITZER OBSERVATIONS OF MASSIVE, RED GALAXIES AT HIGH REDSHIFT[1]

C. Papovich[2,3], L. A. Moustakas[4], M. Dickinson[5], E. Le Floc'h[2,6], G. H. Rieke[2], E. Daddi[3,5], D. M. Alexander[7],
F. Bauer[8], W. N. Brandt[9], T. Dahlen[10,11], E. Egami[2], P. Eisenhardt[4], D. Elbaz[12], H. C. Ferguson[10], M. Giavalisco[10],
R. A. Lucas[10], B. Mobasher[10], P. G. Pérez–González[2], A. Stutz[2], M. J. Rieke[2], AND H. Yan[13]
Accepted for Publication in the Astrophysical Journal

ABSTRACT

We investigate the properties of massive galaxies at $z \sim 1-3.5$ using *Hubble Space Telescope* observations at optical wavelengths, ground–based near–infrared (IR) imaging, and *Spitzer Space Telescope* observations at 3–24 μm. From K_s–selected galaxies over a $\simeq 130$ arcmin^2 field in the southern Great Observatories Origins Deep Surveys (GOODS–S), we identify 153 distant red galaxies (DRGs) with $(J-K_s)_{\mathrm{Vega}} \geq 2.3$. This sample is approximately complete in stellar mass for passively evolving galaxies above 10^{11} $\mathcal{M}_\odot$ and $z \leq 3$. Of the galaxies identified by this selection, roughly half are objects whose optical and near–IR rest–frame light is dominated by evolved stars combined with ongoing star formation (at $z_{\mathrm{med}} \sim 2.5$), and the others are galaxies whose light is dominated by heavily reddened ($A_{1600} \gtrsim 4-6$ mag) starbursts (at $z_{\mathrm{med}} \sim 1.7$). Very few of the galaxies ($\lesssim 10\%$) have no indication of current star formation. The total star–formation rates (SFRs) including the reradiated IR emission for the DRGs are up to two orders of magnitude higher than those derived from the UV luminosity corrected for dust reddening. We use population synthesis models to estimate stellar masses and to study the stars that dominate the rest–frame UV through near–IR light in these galaxies. DRGs at $z \sim 1.5-3$ with stellar masses $\geq 10^{11}$ $\mathcal{M}_\odot$ have specific SFRs (SFRs per unit stellar mass) ranging from 0.2 to 10 Gyr^{-1}, with a mean value of ~ 2.4 Gyr^{-1}. Based on the X–ray luminosities and rest–frame near–IR colors, as many as one–quarter of the DRGs may contain AGN, implying that the growth of supermassive black holes coincides with the formation of massive galaxies at $z \gtrsim 1.5$. The DRGs with $\mathcal{M} \geq 10^{11}$ $\mathcal{M}_\odot$ at $1.5 \leq z \leq 3$ have integrated specific SFRs greater the global value over all galaxies at this epoch. In contrast, we find that galaxies at $z \sim 0.3-0.75$ with $\mathcal{M} \geq 10^{11}$ $\mathcal{M}_\odot$ have integrated specific SFRs less than the global value, and more than an order of magnitude lower than that for massive DRGs at $z \sim 1.5-3$. At $z \lesssim 1$, lower–mass galaxies dominate the overall cosmic mass assembly. This suggests that the bulk of star formation in massive galaxies occurs at early cosmic epochs and is largely complete by $z \sim 1.5$. Further mass assembly in these galaxies takes place with low specific SFRs.

Subject headings: cosmology: observations — galaxies: evolution — galaxies: formation — galaxies: high-redshift — galaxies: stellar content — infrared: galaxies

[2] Steward Observatory, University of Arizona, 933 North Cherry Avenue, Tucson, AZ 85721; papovich@as.arizona.edu

[3] Spitzer Fellow

[4] Jet Propulsion Laboratory, California Institute of Technology, Mail Stop 169-327, 4800 Oak Grove Dr, Pasadena, CA 91109

[5] National Optical Astronomy Observatory, 950 North Cherry Avenue, Tucson, AZ 85721

[6] Associated to Observatoire de Paris, GEPI, 92195 Meudon, France

[7] Institute of Astronomy, Madlingley Road, Cambridge CB30HA, UK

[8] Chandra Fellow, Columbia Astrophysics Laboratory, Columbia University, 500 W. 120th St., New York, NY 10027

[9] Department of Astronomy and Astrophysics, 525 Davey Laboratory, Pennsylvania State University, University Park, PA 16802

[10] Space Telescope Science Institute, 3700 San Martin Drive, Baltimore, MD 21218

[11] Department of Physics, Stockholm University, SE-106 91, Stockholm, Sweden

[12] CEA Saclay/Service d'Astrophysique, Orme des Merisiers, F-91191 Gif-sur-Yvette Cedex, France

[13] Spitzer Science Center, California Institute of Technology, MS 220-6, Pasadena, CA 91125

1. INTRODUCTION

Most of the stellar mass in galaxies today apparently formed during the relatively short period between $z \sim 3$ and 1 (e.g. Dickinson et al. 2003; Rudnick et al. 2003; Fontana et al. 2004; Glazebrook et al. 2004). Some early–type galaxies appear as soon as $z \sim 1.5-2$ (Dunlop et al. 1996; Spinrad et al. 1997; McCarthy et al. 2004; Daddi et al. 2005a). By $z \sim 1$, there is a significant population of galaxies with red colors and morphologies consistent with passively–evolving early–type galaxies, implying they formed their stellar populations at $z_{\mathrm{form}} \gtrsim 2-3$ (e.g., Cimatti et al. 2002a; Moustakas & Somerville 2002; Moustakas et al. 2004; Papovich et al. 2005; Treu et al. 2005; McCarthy 2004, for a review). The cosmic star–formation rate (SFR) density has declined by roughly a factor 10 from $z \sim 1$ to the present–day (e.g. Hopkins 2004, and references therein). During the time since $z \sim 1$ the stellar mass in passively–evolving, early–type galaxies has increased by less than a factor 2 (e.g. Brinchmann & Ellis 2000; Bell et al. 2004), and at the present epoch, roughly one–third of all stars exist in such galaxies (Baldry et al. 2004).

Although massive galaxies appear to have formed most of their stars at epochs prior to $z \sim 1-2$, we have few constraints on how they assembled their stellar mass. One hypothesis is that galaxies "downsize" and star formation

shifts from galaxies at the high to the low end of the mass function with decreasing redshifts (e.g., Cowie et al. 1999; Fontana et al. 2003; Heavens et al. 2004; Kauffmann et al. 2004; Bauer et al. 2005; Caputi et al. 2005; Juneau et al. 2005; Pérez–González et al. 2005). Another possibility is that massive galaxies assemble their stellar mass early–on, either *in situ*, "closed–box" formation events with subsequent passive evolution (e.g., Eggen, Lynden–Bell, & Sandage 1962), or in low–mass systems, which then coalesce to form large galaxies with little subsequent star formation (e.g., Baugh et al. 1998; Kauffmann & Charlot 1998; Cimatti et al. 2002b).

Testing these proposals has been frustrated by difficulties in conducting a complete census of star–forming galaxies and massive galaxies at $z \gtrsim 2$, when such systems are expected to experience a peak in their stellar assembly rates (e.g. De Lucia et al. 2005; Nagamine et al. 2005). Ultraviolet (UV)–luminous star–forming galaxies at these redshifts are identified by the characteristic "break" in their colors due to neutral hydrogen absorption that attenuates the flux shortward of Lyman α (1216 Å) and the 912 Å Lyman limit (e.g. Steidel et al. 1996; Giavalisco 2002, for a review). These UV–dropout, Lyman–break galaxies (LBGs) dominate the UV luminosity density at $z \sim 2-6$, and possibly the global SFR density at these redshifts (e.g., Steidel et al. 1999; Bouwens et al. 2004; Giavalisco et al. 2004b). However, the UV–dropout technique is primarily sensitive to galaxies with ongoing, relatively unreddened star formation. Surveys with SCUBA have identified a population of sub–mm galaxies at $z \gtrsim 2$ that emit the bulk of their bolometric luminosity at infrared (IR) wavelengths (see Blain et al. 2002, for a review), and may contribute substantially to the cosmic SFR (Barger et al. 2000). Their inferred space densities and SFRs suggest that they could be the progenitors of the most massive present–day galaxies (Blain et al. 2004; Chapman et al. 2005). Neither the LBG nor the sub-mm–galaxy populations necessarily provide a full sample selected by stellar mass, so how they participate in the formation of present–day massive galaxies is poorly understood. Hence, it is unclear what fraction of present–day galaxies pass through such stages during their assembly.

Theoretically, the star–formation histories of massive galaxies are also poorly known. Galaxies within massive halos have short cooling times and tend to convert all their gas into stars rapidly, unless feedback is invoked from stellar winds and supernovae to reheat the gas or prevent it from cooling (e.g. Hernquist & Springel 2003; Springel et al. 2005a,b). Models predict that massive galaxy halos continue to accrete smaller aggregates up to the current epoch, which rejuvenates star–formation and predicts galaxy colors that are too blue compared to observations (e.g. Somerville, Primack, & Faber 2001) unless very large dust extinctions or non–standard stellar initial mass functions (IMFs) are invoked (Baugh et al. 2005; Nagamine et al. 2005). Some recent theoretical models suppress star–formation at late times in massive galaxies using feedback from active–galactic nuclei (AGN; Granato et al. 2001; Di Matteo et al. 2005; Hopkins et al. 2005; Springel et al. 2005a). This process may provide the impetus for the present–day black-hole–bulge-mass correlation (Magorrian et al. 1998; Gebhardt et al. 2000; Kauffmann et al. 2004). We require observations of star–formation and AGN activity in high–redshift, massive galaxies to improve our understanding of how such systems form.

Surveys using deep, near–IR observations have identified high–redshift, massive–galaxy candidates with red near–IR colors (e.g., Dickinson et al. 2000; Totani et al. 2001; Im et al. 2002; Daddi et al. 2004; Yan et al. 2004a). Franx et al. (2003) used deep JHK_s observations from VLT/ISAAC to identify a population of galaxies with $(J-K_s)_{\rm Vega} > 2.3$ mag in the Faint IR Extragalactic Survey (FIRES). In principle, this color selection identifies galaxies that have a strong Balmer/4000 Å break between the J and K_s bands at $z \sim 2-3.5$, down to an approximately complete limit in stellar mass. Subsequent analysis has concluded that these distant red galaxies (DRGs) are mostly massive, old, and actively forming stars at $z \sim 1.5-3.5$ (van Dokkum et al. 2003; Förster–Schreiber et al. 2004; Rubin et al. 2004; Knudsen et al. 2005; Reddy et al. 2005) although some appear to be completely devoid of star–formation and passively evolving (Labbé et al. 2005), while others appear to host powerful AGN (van Dokkum et al. 2004). The inferred stellar masses of DRGs at $z \sim 2-3$ are similar to those of local early–type galaxies (Förster–Schreiber et al. 2004). They are generally higher than those inferred from LBG samples at similar redshifts (Sawicki & Yee 1998; Papovich, Dickinson, & Ferguson 2001; Shapley et al. 2001), although some overlap between the two clearly exists (Shapley et al. 2005; Reddy et al. 2005). The estimated stellar population ages of the DRGs suggests that they have been forming stars since $z \sim 5-6$ (Förster–Schreiber et al. 2004). Thus DRGs may represent the older stellar populations formed in higher–redshift LBGs (e.g. Papovich et al. 2004a), and these galaxies possibly link the UV–luminous LBGs to the sub–mm galaxies (van Dokkum et al. 2004).

In addition, extinction may contribute to the red colors of some of the galaxies. Smail et al. (2002) find that dust–extincted starbursts at $z \sim 1-2$ selected as extremely red objects (EROs) typically have red $J-K$ colors similar to DRGs. Using current hierarchical model predictions, Nagamine et al. (2005) suggest that massive galaxies in formation at $z \gtrsim 1$ may be heavily reddened by dust. If so, then most of their emission should appear in the thermal IR. In fact, up to half of EROs (selected with red $R-K$ or $R-[3.6\mu m]$ colors) at $z \gtrsim 1$ are detected in the thermal IR by *Spitzer*/MIPS at 24 μm (Wilson et al. 2004; Yan et al. 2004b). In addition, the inferred evolution of the galaxy population responsible for the IR number counts implies a substantial population of galaxies at $z \sim 1-3$ (Papovich et al. 2004b; Caputi et al. 2005; Pérez–González et al. 2005), and the evolution in the IR luminosity function suggest that luminous IR galaxies (LIRGs, $L_{\rm IR} = 10^{11-12} L_{\odot}$), and ultraluminous IR galaxies ($L_{\rm IR} \geq 10^{12} L_{\odot}$) dominate the IR luminosity density at $z \gtrsim 1$ (Le Floc'h et al. 2005; Pérez–González et al. 2005).

For this study, we selected galaxies at $z \sim 1-3.5$ with $(J-K_s)_{\rm Vega} > 2.3$ mag ($[J-K_s]_{\rm AB} > 1.37$ mag) from a K_s–band selected catalog in the southern Great Observatories Origins Deep Survey (GOODS-S) field. At the magnitude limit of $K_s \leq 23.2$ [AB], this sample is approximately complete in stellar mass for passively evolving galaxies with $\mathcal{M} > 10^{11} \mathcal{M}_{\odot}$ for $z \leq 3$. We also use IR and X–ray observations to constrain the star–formation and AGN processes in these galaxies. The AGN connection in these galaxies is explored in more detail in a forthcoming paper (L. A. Moustakas et al., in preparation). In § 2, we summarize the data and we define the galaxy samples. In § 3, we describe broad properties of the DRGs using their rest–frame UV to near–IR colors. In § 4,

we compare the IR luminosities for the galaxies with those derived from their UV luminosity and measured extinction, and we compare the DRGs to other galaxies at $1.5 \leq z \leq 3.5$. In § 5, we use population synthesis models to estimate the properties of the galaxies' stellar populations. In § 6, we discuss the relationship between the SFRs and stellar population properties for the ensemble of galaxies, and we comment on the presence of AGN. We also compare the distribution of SFR as a function of galaxy stellar mass at high redshift, and we compare with results at lower redshifts ($z \sim 0.3 - 0.75$). In § 7 we present our conclusions.

Throughout this paper we use a cosmology with $\Omega_{\mathrm{Total}} = 1$, $\Omega_{\mathrm{M}} = 0.3$, $\Lambda = 0.7$, and $H_0 = 70$ km s^{-1} h_{70} Mpc^{-1} where $h_{70} \equiv 1$. Unless otherwise specified, we present all magnitudes in the AB system, $m_{\mathrm{AB}} = 23.9 - 2.5 \log(f_\nu / 1 \ \mu\mathrm{Jy})$. We denote galaxy magnitudes from the *HST* ACS bandpasses F435W, F606W, F775W, and F850LP as B_{435}, V_{606}, i_{775}, and z_{850}, respectively. Similarly, where applicable we denote magnitudes from the *HST* WFPC2 and NICMOS bandpasses F300W, F450W, F606W, F814W, F110W, and F160W as U_{300}, B_{450}, V_{606}, I_{814}, J_{110}, and H_{160}, respectively. We also denote magnitudes from the four *Spitzer* IRAC channels as [3.6μm], [4.5μm], [5.8μm], and [8.0μm], respectively.

2. THE DATA AND SAMPLE DEFINITIONS

The GOODS–S field center is located in the southern *Chandra* Deep X–ray field (CDF–S) at $3^{\mathrm{h}}32^{\mathrm{m}}30^{\mathrm{s}}$, $-27°48'20''$, which provides 1 Ms of imaging in the soft (0.5–2 keV) and hard (2–8 keV) X–ray bands in this field. The available observations include imaging with *HST*/ACS in four passbands, B_{435}, V_{606}, i_{775}, and z_{850} over 160 arcmin^2, ground–based near–IR imaging from VLT/ISAAC in the JK_s bands over 130 arcmin^2 (with H–band imaging over $\simeq$ 50 arcmin^2), and IR imaging from *Spitzer*/IRAC in four bands, [3.6μm], [4.5μm], [5.8μm], [8.0μm].

The ACS observations and data reduction are described in Giavalisco et al. (2004a). The images have a PSF FWHM $\simeq 0.''125$, and the limiting 10σ sensitivities are $B_{435} = 27.8$, $V_{606} = 27.8$, $i_{775} = 27.1$, $z_{850} = 26.6$, measured in $0.''2$–diameter circular apertures. The *Spitzer*/IRAC images have a PSF FWHM ranging from $\simeq 1.''5$ at 3.6 μm to $\simeq 2''$ at 8 μm, and for isolated point sources achieve 5σ limiting sensitivities ranging from 0.11 μJy at 3.6 μm to 1.66 μJy at 8 μm (M. Dickinson, et al., in preparation).

The near–IR ISAAC imaging is from the version 1.0 release (B. Vandame et al., in preparation), available on the ESO/GOODS webpages.[14] The ISAAC data have excellent image quality (full–width at half maximum, FWHM $\approx 0.''45$) with mean exposures times of 14000 and 24000 s in J and K_s, respectively, reaching limiting magnitudes of $J = 24.7$, $H = 24.1$ and $K_s = 24.1$ (10σ) in $1''$–diameter apertures, although the depth varies over the GOODS–S field.

Spitzer imaged the CDF–S field with MIPS at 24, 70, and 160 μm under *Spitzer*/Guaranteed Time Observer (GTO) time. Here, we focus exclusively on the 24 μm imaging, which was reduced using the instrument team Data Analysis Tool (Gordon et al. 2005). The GTO MIPS imaging covers $1° \times 0.5°$ with a FWHM ≈ 6 arcsec, and covers all of the GOODS–S field and most of the ESO imaging and COMBO–17 surveys (see § 2.5).

2.1. *GOODS Source Cataloging and DRG Sample Selection*

We use a source catalog selected from the ISAAC K_s–band data. We rebinned the ACS data to the pixel scale of ISAAC, and convolved the ACS images to match the image quality of the ISAAC images. Source catalogs were then constructed using the SExtractor software (Bertin & Arnouts 1996) by first locating sources on the K_s–band image, then measuring photometry in matched apertures on the *HST*/ACS and ISAAC images. We measured photometry in each band in isophotal apertures defined from the K_s–band image. We then scaled these to total magnitudes using the difference between the K_s–band isophotal magnitude (SExtractor MAG_ISO) and the K_s–band magnitude measured in a "total", elliptical aperture defined by the Kron radius (SExtractor MAG_AUTO). Photometric uncertainties are derived by SExtractor after adjusting the image rms maps to account for the correlated noise properties introduced by drizzling.[15] The SExtractor–derived uncertainties still likely underestimate the true errors, because they do not account for systematic errors in the measurements themselves. Therefore, we have included an additional error of $\sigma_{\mathrm{sys}} / f_\nu \approx 3\%$, added in quadrature to the uncertainties on the ACS and ISAAC photometry.

We detected objects in the *Spitzer*/IRAC images using a weighted–sum image of IRAC channels 1 and 2. Magnitudes were then measured in each IRAC band in $4''$–diameter apertures, and we applied aperture corrections of 0.30, 0.34, 0.53, and 0.67 mag to the bands [3.6μm], [4.5μm], [5.8μm], and [8.0μm], respectively, to correct to total magnitudes. We did not attempt to measure photometry on versions of the ISAAC data PSF–matched to the IRAC data, because of the significantly poorer image quality of the IRAC data. The aperture corrections are based on Monte Carlo simulations using artificial, compact sources added to the real images, and are appropriate for sources with half–light radii $< 0.''5$, such as those of interest here. These simulations also allow us to estimate the error on the IRAC photometry as a function of flux density. The uncertainties are similar for IRAC channels 1 and 2, and range from $\Delta m \approx 0.03$ mag at $m \approx 21$ mag to $\Delta m \approx 0.3$ mag at $m \approx 25$ mag. For IRAC channels 3 and 4, they range from $\Delta m \approx 0.05$ mag at $m \approx 21$ mag to $\Delta m \approx 0.4$ mag at $m \approx 25$ mag.

We used $(J - K_s)_{\mathrm{Vega}} > 2.3$ mag to identify DRGs. In the GOODS–S field, we found 153 of them to a signal–to–noise ratio S/N(K_s) ≥ 10 limit, which is the median S/N of objects at $K_s \leq 23.2$ mag within the "total", MAG_AUTO apertures, and with $J - K_s$ colors measured in the seeing–matched MAG_AUTO apertures. Restricting sources to the S/N requirement is appropriate as the ISAAC depth varies over the GOODS–S field. Using a S/N limit also ensures that we can derive robust colors from the ACS and ISAAC data, greatly improving the accuracy of our SED modeling and photometric redshifts. We inspected the ACS image for each DRG at their native resolution to identify objects resulting from chance galaxy–galaxy alignments along the line of sight. In one case the DRG does appear to involve multiple ACS sources, blended at the K–band resolution. We exclude this object although its inclusion does not effect the results in this paper. A unique IRAC source exists for 132 of the 153 DRGs with a matching radius of $r \leq 0.''5$. We visually inspected each object to verify that the matched IRAC source corresponds to the DRGs in the K_s–band image. The unmatched objects suffer from crowding in the IRAC images from other sources within $\simeq 1$–$2''$. The IRAC flux from these non–detected
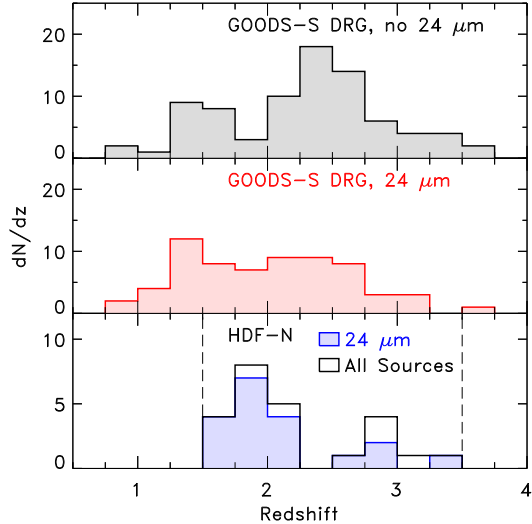
FIG. 1.— Distribution of redshifts for the DRG and HDF–N galaxy samples. The top panel shows the redshift distribution of DRGs with no 24 μm detections. The middle panel shows the redshift distribution of DRGs with $f_\nu(24\mu m) \geq 50$ μJy. The bottom panel shows the redshift distribution of the 24 galaxies from the HDF–N with $1.5 \leq z \leq 3.5$ and $K_s \leq 23.2$ mag. The dashed lines indicate the redshift limits of the sample. The shaded histogram shows the distribution for those HDF–N galaxies with $f_\nu(24\mu m) \geq 10$ μJy.

DRGs is either completely blended within the isophote of the neighbor, or confusion with the neighbor offsets the centroid of the IRAC flux past the matching criterion.

Spectroscopic redshifts are available for 12 of the DRGs (Szokoly et al. 2004; Mignoli et al. 2005; Vanzella et al. 2005; D. Stern 2005, private communication). We therefore supplement the redshift information using photometric redshifts from Mobasher et al. (2004 and in preparation). The high–quality dataset allows for accurate photometric redshifts. The median photometric–redshift uncertainty for all K_s–band sources with spectroscopic redshifts is $\delta z/(1+z) \simeq 0.1$, similar to the accuracy found by Caputi et al. (2005) using similar data in the same field. For the 12 DRGs with spectroscopic redshifts, the photometric–redshift accuracy is even better, $\langle \delta z/(1+z) \rangle \simeq 0.04$. A photometric redshift is unavailable for one of the DRGs, whose ACS and ISAAC J–band photometry have S/N< 1. We ignore this DRG for any analysis requiring a redshift (e.g., luminosities, stellar masses, etc.). Figure 1 shows the redshift distribution. The redshifts range from $z \simeq 0.8 - 3.7$, with a median redshift $\langle z \rangle = 2.2$. This is in broad agreement with the redshift distribution for DRGs reported in the FIRES surveys (Franx et al. 2003; Förster–Schreiber et al. 2004), although there is a larger fraction of DRGs with $z \lesssim 2$ in the GOODS–S field compared to the FIRES samples (see § 3). We believe the lower median redshift of the GOODS–S DRGs primarily results from the larger areal coverage combined with the somewhat brighter flux limit of the GOODS–S field. In addition, cosmic variance between the GOODS–S and FIRES fields may contribute to this difference.

However, roughly 20% (30/152) of the DRGs have redshifts $z \leq 1.5$ (including two with spectroscopic redshifts), significantly lower than the typical redshifts reported for the FIRES samples.[16] We have inspected the SEDs of this low–redshift

[16] van Dokkum et al. (2003) find that one of the six DRGs in their spec-

DRG subsample and found that the ACS through IRAC colors supports the derived redshifts with high fidelity for the majority (27/30) of galaxies. For these DRGs, the IRAC photometry shows a fairly robust turnover at rest–frame 1.6 μm near the expected peak in the stellar emission, and the SEDs at the inferred redshift are otherwise consistent with the ACS and ISAAC colors. In the remaining three cases, their ACS photometry has low S/N, leading to dubious results. Ignoring these three galaxies has no effect on the analysis and conclusions derived here, but we include them in the sample for completeness. In § 6, we conclude that the lower redshift ($z \lesssim 2$) DRGs are mostly heavily extincted starbursts, and are probably part of the class of dusty EROs at $z \gtrsim 1$, which typically have red $J-K_s$ colors that satisfy the DRG selection criterion (Smail et al. 2002; Franx et al. 2003).

2.2. *Spitzer 24 μm Source Detection and Cataloging*

Papovich et al. (2004b) describe the data reduction and point–source photometry methods applied to the *Spitzer*/MIPS 24 μm image. They show that the GTO 24 μm data reach a 50% completeness limit at 60 μJy. We reanalyzed the simulations discussed in Papovich et al. to estimate the flux uncertainties as a function of MIPS 24 μm flux density. The median 24 μm S/N is ≈ 4 for objects with $f_\nu(24\mu m) = 80 - 90$ μJy (the 80% completeness limit). We cross–correlated 24 μm sources with $f_\nu(24\mu m) \geq 50$ μJy (the S/N ≈ 3 limit) to the K_s–band catalog and identified matches with a radius of $2''$. Roughly one–half (74/153) of the DRGS are detected by *Spitzer*/MIPS at 24 μm. The majority of these 24 μm–detected DRGs (71/74) have IRAC counterparts associated with each DRG in the K_s–band image. The remaining three appear associated with IRAC sources at distances $0''\!.5 \leq r \leq 2''\!.0$ from the K_s–band source. For the source density at the flux limit of the 24 μm data (Papovich et al. 2004b), we expect a random–association probability of 0.03 within a $2''$ radius, which is consistent with the three sources with no IRAC counterpart. Therefore, these sources are likely change alignments.

Figure 1 shows the redshift distribution of the DRGs detected at 24 μm. The distribution of this sub–population is similar to those DRGs not detected at 24 μm, except for an apparent spike in the redshift distribution at $z \simeq 2.2$ for the 24 μm–undetected DRGs. The 24 μm–detected DRGs have a mean redshift $\langle z \rangle = 2.0$, slightly lower than the mean redshift for the DRGs with no 24 μm detection, $\langle z \rangle = 2.3$. Using a Kolmogoroff–Smirnov statistic, there is a moderate likelihood (90% confidence) that the two sub–populations of DRGs are drawn from different parent samples. Different redshift distributions in part may arise because the 24 μm subsample includes a large number of lower–redshift galaxies. However, at $z \sim 2$ the 7.7 μm emission feature from polycyclic aromatic hydrocarbons (PAHs) lies in the 24 μm bandpass, and thus one might expect *more* IR–detected galaxies to appear. The sharp increase in the number of 24 μm–undetected DRGs at $z \simeq 2.2$ may result from the fact that at this redshift the DRG selection begins to pick up galaxies with strong Balmer/4000 Å breaks that shift between the J and K_s–bands. Such galaxies presumably have low specific SFRs (SFR per unit stellar mass), and perhaps have lower IR emission, so fewer would be detected at 24 μm.

troscopic sample has $z_{spec} = 1.19$. They estimate that the red $J-K_s$ color selection has a $\sim 20\%$ contamination of (dusty) galaxies at lower redshift, probably consistent with the fraction of DRGs at $z \leq 1.5$ in our sample.

2.3. *X–ray Source Detection and Cataloging*

The CDF-S has aim–point flux limits (S/N= 3) in the 0.5–2.0 keV and 2–8 keV bands of $\approx 2.5 \times 10^{-17}$ erg cm^{-2} s^{-1} and $\approx 1.4 \times 10^{-16}$ erg cm^{-2} s^{-1}, respectively. The completeness limit over $\approx$ 90% of GOODS-S field is $\approx 1.3 \times 10^{-16}$ erg cm^{-2} s^{-1} (0.5–2.0 keV) and $\approx 8.9 \times 10^{-16}$ erg cm^{-2} s^{-1} (2–8 keV). Assuming an X–ray spectral slope of $\Gamma = 2.0$, a source detected with a flux of $\approx 10^{-16}$ erg cm^{-2} s^{-1} would have both observed and rest frame luminosities of $\approx 5.2 \times 10^{41}$ erg s^{-1} and $\approx 7.6 \times 10^{42}$ erg s^{-1} at $z = 1$ and $z = 3$, respectively, assuming no Galactic absorption.

In this study we use the main and supplementary *Chandra* catalogs of Alexander et al. (2003). The median positional accuracy for the sources in the GOODS-S field in the main *Chandra* catalog is $0.''6$. We matched all K_s–band sources to the X–ray catalog within a radius of $1''$ and identified all matches in both the soft– and hard–band catalogs. Nearly one–seventh (22/153) of the DRGs have X–ray detections in either the soft or hard bands (or both). Of these, 12 are detected at 24 μm, while the remaining 10 are not. All of the X–ray detected DRGs have IRAC counterparts.

2.4. *High–Redshift Sample of IR–luminous Galaxies from the HDF–N*

We construct a comparison sample of galaxies within the northern Hubble Deep Field (HDF–N, Williams et al. 1996), which spans all types of galaxies (not just the reddest galaxies identified by the DRG–selection), and extends our analysis to fainter 24 μm fluxes. This allows us to study how the DRGs are drawn from the general galaxy population at similar redshifts. Galaxies were selected from the NICMOS HDF catalog of M. Dickinson et al. (Dickinson et al. 2000; Papovich, Dickinson, & Ferguson 2001; Dickinson et al. 2003), and matched to the deep IRAC and MIPS 24 μm observations of the northern GOODS (GOODS–N) field (M. Dickinson et al., in preparation; R. Chary et al., in preparation). From the NICMOS–selected catalog, we identify 24 galaxies in the HDF–N with $K_s \leq 23.2$ mag and redshift, $1.5 \leq z \leq 3.5$, roughly in the same range as in the GOODS–S DRGs. Spectroscopic redshifts are available for 13 of the galaxies in this sample (see Dickinson et al. 2003, and references therein). For the remaining 11 galaxies, we use the photometric redshift catalog from Budavári et al. (2000). Of this sample, 19 are detected with the MIPS 24 μm imaging to $f_\nu(24\mu m) \geq 10$ μJy.

Figure 1 shows the redshift distribution of the HDF–N galaxies. We note that four of these galaxies with $K_s \leq 23.2$ mag have $(J_{110} - K_s)_{AB} > 1.6$, and possibly satisfy the DRG color criterion (allowing for differences in the HDF–N and GOODS–S filter sets). Of these, three have $f_\nu(24\mu m) \geq 50$ μJy, and so could have been detected in the 24 μm of the CDF–S.

2.5. *Low–Redshift Galaxy Samples from COMBO–17*

In § 6, we compare the SFRs and stellar masses of the high–redshift DRGs to those of lower–redshift samples. The GTO *Spitzer*/MIPS 24 μm imaging intersects roughly 700 arcmin^2 of the COMBO–17 survey (Wolf et al. 2003) in a substantially larger region encompassing the 130 arcmin^2 GOODS–S field. COMBO–17 provides photometric redshifts for galaxies with $R \lesssim 23.5$ mag to $z \lesssim 1.3$ (Wolf et al. 2004). Where possible, we replaced many of these photometric redshifts with spectroscopic ones (Le Fèvre et al. 2004; Vanzella et al. 2005). We then constructed samples of galaxies with $R \leq 23.5$ mag in two redshift slices, $0.3 \leq z < 0.5$ and $0.65 \leq z < 0.75$. We cross–correlate the COMBO–17 catalogs with the GTO MIPS 24 μm catalogs to identify matches within a $2''$ radius. We find 1495 galaxies in the full $z \sim 0.7$ sample, of which 464 are detected in the MIPS 24 μm catalog to 24 μm 50% completeness flux limit. Similarly, there are 1269 sources in the full $z \sim 0.4$ sample, with 276 sources detected in the MIPS 24 μm catalog (see also the discussion in Bell et al. 2005; Le Floc'h et al. 2005). Each sample contains approximately the same co-moving volume in these redshift intervals ($\simeq 10^6 h_{70}^3$ Mpc^3), although we find relatively fewer objects at $z \sim 0.4$ than $z \sim 0.7$ to the same magnitude limit. This results from large–scale clustering in this field, which is known to be underdense at $z \sim 0.4$ (Wolf et al. 2003). While IRAC imaging also exists for most of the COMBO–17 field, we have not included it in our analysis of the galaxy stellar masses as it provides observations longward of rest–frame 2 μm, past the peak of the stellar emission (see discussion in § 6.4).

3. THE REST–FRAME OPTICAL AND NEAR–IR COLORS OF DRGS

Galaxies at $z \sim 2 - 3.5$ with a strong 4000 Å/Balmer break should have colors that satisfy the $(J - K_s)_{\rm Vega} > 2.3$ mag criterion (Franx et al. 2003). This color selection is also sensitive to starburst galaxies at $z \gtrsim 1$ whose light is heavily obscured by dust. Förster–Schreiber et al. (2004) note evidence for both galaxy types in the $I_{814} - J_s$, $J_s - H$, and $H - K_s$ color distributions of DRGs, which is similar to the reputed nature of BzK–selected objects Daddi et al. (2004). We find that the full rest–frame UV to near–IR colors of DRGs provide further support for this dual population.

In Figure 2 we compare the SEDs of the GOODS–S DRGs with empirical and theoretical UV–IR SEDs for local galaxies. The DRGs have colors that fit within the envelope defined by various galaxy types. Many of the DRGs have colors close to the locus of that for early–type galaxies. There is also a class of DRG with optical colors redder than even the elliptical template of Coleman et al. (1980). Most of them are 24 μm sources, and they have very red UV–optical rest–frame colors, consistent with dust–obscured starbursts. The flux ratio between the 24 μm and near–IR emission is consistent with that of galaxies with massive starbursts, such as the local ULIRG Arp 220. Most of the DRGs show a prominent inflection in their SEDs at rest–frame 1.6 μm as expected in the SEDs of galaxies dominated by the light of composite stellar populations (e.g., Simpson & Eisenhardt 1999; Sawicki 2002). The ensemble DRG photometry in the mid–IR shows slight evidence for a peak at ~ 8 μm rest–frame coincident with the PAH 7.7 μm emission feature, suggesting that the emission from the majority of DRGs stems from stellar processes rather than nuclear activity. There is a slight decline in the flux density at $9 - 10$ μm, possibly consistent with silicate absorption, which is observed in both starburst galaxies and AGN. A small subset of the DRGs have red colors around $\lambda \sim 1 - 5$ μm rest–frame, a signature of AGN emission (e.g., Rieke 1978; Neugebauer et al. 1979, and discussion in § 6.3).

In Figure 3, we show an optical and near–IR color–color diagram to study the stellar populations and dust extinction in the DRGs. The simple models plotted in the figure bound the range of colors observed in the GOODS–S DRGs, comparable to the findings of Labbé et al. (2005) for a smaller FIRES sample. DRGs with the blue $K_s - [4.5\mu m]$ colors require a substantial population of mature stellar populations with a strong 4000 Å/Balmer break, which produces the
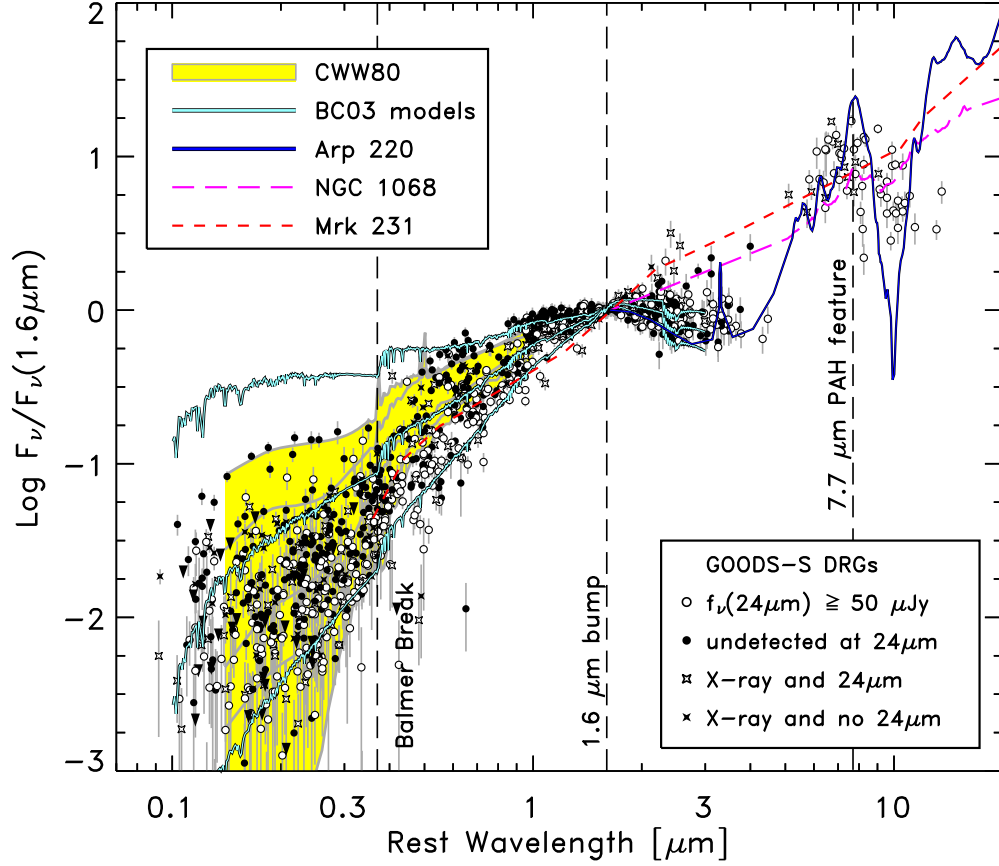
FIG. 2.— Ensemble photometry of the DRGs in the GOODS–S sample. The data points are the measured flux densities from the ACS (B_{435}, V_{606}, i_{775}, z_{850}), ISAAC (J, H, K_s), IRAC ([3.6μm], [4.5μm], [5.8μm], [8.0μm]), and MIPS 24 μm images, normalized to a common flux density at 1.6 μm rest–frame. Open symbols show the photometry for galaxies detected at 24 μm with MIPS, and solid symbols show galaxies with no 24 μm detection. Stars correspond to galaxies detected in the X–ray data. The shaded region is defined by the SEDs for ordinary galaxies from Coleman, Weedman, & Wu (1980; CWW80), and span Hubble types from elliptical galaxies through Sab, Sbc, and Scd spirals, to the bluest Magellanic irregular, Im, templates. The solid cyan curves show the SEDs from 0.1 to 3 μm for stellar populations from the Bruzual & Charlot (2003; BC03) formed with constant star formation for 100 Myr with dust extinction of 1.5, 4.5, and 7.5 mag at 1600 Å using the Calzetti et al. (2000) extinction law. The solid blue curve shows the SED of the local ULIRG Arp 220 from an empirical model for $1-5$ μm (Silva et al. 1998) and a composite spectrum covering $5-3000$ μm (Spoon et al. 2004). The latter shows the prominent PAH emission feature at 7.7 μm, and silicate absorption at 9.7 μm. The short–dashed, red curve shows the SED of the local ULIRG and AGN Mrk 231, and the long–dashed magenta curve shows that for the local Seyfert 2 galaxy NGC 1068 (Le Floc'h et al. 2001), both of which rise smoothly through the near– and mid–IR.

red $J-K_s$ color. DRGs with redder $K_s - [4.5\mu m]$ colors require ongoing star formation with substantial dust extinction. Changes in the redshift of the model stellar populations from $z = 2.2$ to 3.5 or 1.5 shift the expected colors by ± 0.3 mag in $K_s - [4.5\mu m]$ mag, respectively, but have little effect on the $i_{775} - K_s$ colors. The models bound the majority of the colors of the DRGs (with the exception of several X–ray sources, whose optical to near–IR colors are possibly influenced by AGN). Thus, the colors of the DRGs imply a mix of old and young stellar populations, in some cases with substantial extinction. The MIPS 24 μm data support this interpretation. The top panel of Figure 3 shows the $K_s - [4.5\mu m]$ colors of the DRGs detected at 24 μm and those with no 24 μm detection. The DRGs with 24 μm detections have redder $K_s - [4.5\mu m]$ colors, suggesting that the emission from many DRGs is attenuated by a large dust opacity.

Of the sample of 132 DRGs with IRAC detections, there are only 6–9 DRGs (within the photometric uncertainties) that have $i_{775} - K_s \geq 4$ mag and $K_s - [4.5\mu m] < 1.5$ mag (including two sources with 24 μm detections and one X–ray source). These color thresholds should identify passively

evolving galaxies with ages greater than ≈ 0.75 Gyr over the redshift range $z \sim 2-3$, and these colors bound the "red and dead" DRGs in the FIRES sample from the southern Hubble Deep Field (HDF–S) (Labbé et al. 2005). Assuming the GOODS–S DRGs with these colors are uniformly distributed over the GOODS–S area and redshift range $2 \leq z \leq 3$ implies they have a number density of $0.7 - 2 \times 10^{-6} h_{70}^{-3}$ Mpc^{-3}. This contrasts with Labbé et al. (2005) who found a higher number density, $1.9 \times 10^{-4} h_{70}^{-3}$ Mpc^{-3}, for DRGs in the HDF–S assuming the same redshift interval. The difference between the DRGs in these fields is not removed by relaxing the color–selection criteria further. Based on the full photometry of our DRG sample (see § 5), we find that 15 DRGs ($\sim 10\%$) have best fit models consistent with old ages (> 1 Gyr), little dust ($E[B-V] < 0.1$), and passive evolution. They have $i_{775} - K_s > 2.6$ mag and $K_s - [4.5\mu m] < 1.1$ mag, both somewhat bluer than the original limits. These galaxies suggest that the number density of massive, passively evolving galaxies at $2 \leq z \leq 3$ is $3.2 \times 10^{-5} h_{70}^{-3}$ Mpc^{-3}, still nearly an order of magnitude lower than that in the HDF–S. However, some of the discrepancy likely arises from the fact that the FIRES data
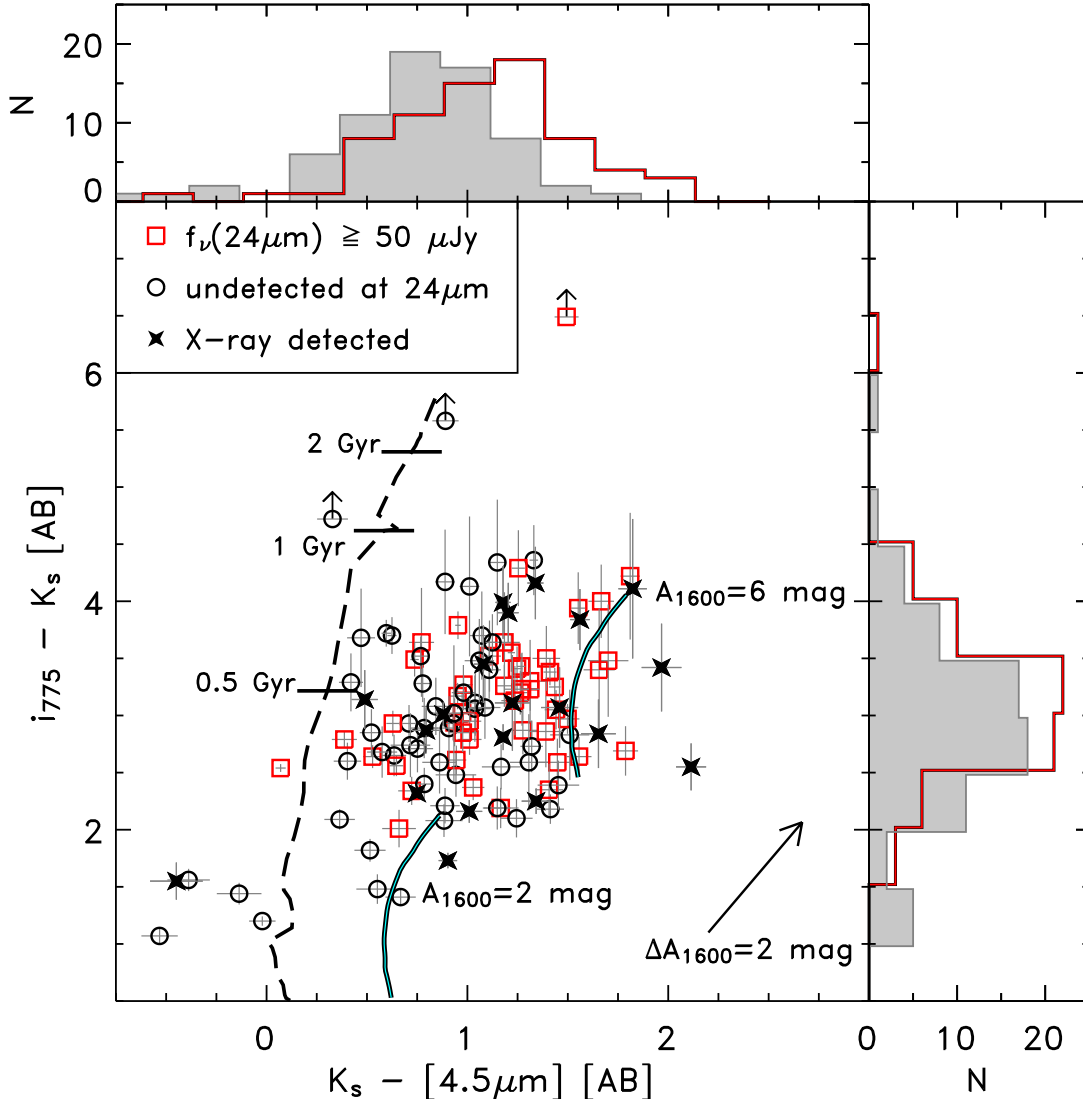
FIG. 3.— The $K_s - [4.5\mu m]$ versus $i_{775} - K_s$, color–color diagram for the GOODS–S DRGs. Symbols show the derived colors from the ACS, ISAAC, and IRAC photometry. Black, open circles show DRGs not detected at 24 μm with MIPS. Red, open squares denote DRGs with 24 μm detections. Filled stars correspond to sources detected in the soft or hard X–ray bands with *Chandra*. Arrows denote upper limits on the ACS $i_{775} - K_s$ colors. The lines show the expected colors of stellar populations at $z = 2.2$ (the median redshift in the DRG sample) using the Bruzual & Charlot (2003) models. The dashed line shows the colors of a passively evolving stellar population formed in a single burst with an age of 50 Myr to 2.8 Gyr; hash marks indicate the colors at ages of 0.5, 1, and 2 Gyr, as labeled. The solid lines show the colors of a stellar population forming with constant star formation for the same ages as above, but with a dust extinction of 2 and 6 mag at 1600 Å, as labeled. The arrow shows the expected differential color for 2 magnitudes of extinction at 1600 Å. The histograms on the top and left panels show the color distributions of those DRGs detected at 24 μm (red solid lines) and undetected at 24 μm (shaded regions).

achieve fainter near–IR flux densities, and parenthetically we note that two of the three candidates for passively evolving DRGs in the Labbé et al. sample have $K_s > 23.2$ mag. Nevertheless, the difference supports the notion that these sources are highly clustered (Daddi et al. 2003), and that the HDF–S itself has an unusual overdensity of them. The low number density of massive, passively evolving galaxies in our sample supports the assertion that the density of passive galaxies is rising strongly at $z < 2$ (see, e.g., Daddi et al. 2005a; Labbé et al. 2005).

There are few DRGs with $i_{775} - K_s \lesssim 2$ (see also, Labbé et al. 2005). Four of the GOODS–S DRGs have $i_{775} - K_s < 2$ and $K_s - [4.5\mu m] < 0$. One of these galaxies is an X–ray source at $z \sim 2.3$ whose colors may be affected by

an AGN. The remaining three have redshifts $z \gtrsim 3$ and relatively flat SEDs from UV to near–IR rest–frame wavelengths. The red $J - K_s$ color arises from a weaker 4000 Å/Balmer break apparently augmented by photometric errors or emission lines in the passbands,[17] which push the J–band fainter and K_s–band brighter by small amounts, and conspire to produce $(J - K_s)_{\rm Vega} > 2.3$ mag. In general we retain these sources in the sample for completeness (although they have a negligible effect on our results). In our analysis below, we also consider a restricted sample with $1.5 \leq z \leq 3.0$, thus excluding

[17] van Dokkum et al. (2004) find small emission–line corrections of $\simeq 0.1 - 0.2$ mag to the K_s–magnitudes in a sample of seven, bright ($K_s[{\rm Vega}] \leq 20$ mag) DRGs.

these objects.

4. TOTAL LUMINOSITIES AND STAR–FORMATION RATES OF HIGH–REDSHIFT GALAXIES

4.1. *Estimating the Total Infrared Luminosities of Star–forming Galaxies*

At the redshifts of the DRGs, $z \sim 1-3.5$, the *Spitzer* 24 μm probes the rest–frame mid–IR, which broadly correlates with the total thermal IR luminosity, $L_{IR} \equiv L(8-1000\mu m)$ (e.g., Spinoglio et al. 1995; Roussel et al. 2001; Chary & Elbaz 2001; Dale et al. 2001; Elbaz et al. 2002; Papovich & Bell 2002). We convert the observed 24 μm flux density to a rest–frame luminosity density at $24/(1+z)$ μm. We then correct these values to a total IR luminosity using the Dale & Helou (2002) IR template SEDs assuming that a given rest–frame IR luminosity density translates uniquely to a single SED template. If we instead used the IR templates of Chary & Elbaz (2001), then we would derive IR luminosities a factor of 2–3 higher relative to those of Dale & Helou for galaxies at $L_{IR} \sim 10^{12.5-13}$ $L_\odot$ (with smaller differences for lower–luminosity galaxies). A recent study of IR–luminous galaxies at $z < 1.2$ indicates that IR–luminosities estimated from the Chary & Elbaz models have a scatter of a factor of two compared to IR luminosities derived from the radio–far-IR correlation (Marcillac et al. 2005). In contrast, the IR luminosities estimated using the Dale & Helou models provide a tighter correlation with IR–luminosities derived from the radio–far-IR correlation, with a scatter of 40%, suggesting these templates possibly better reflect reality. Some scatter is inherent in this estimation of the total IR luminosity: Chapman et al. (2003) find that the temperature–luminosity distribution in IR–luminous galaxies has a scatter of roughly a factor of 2–3 in IR luminosity for galaxies with fixed dust temperature. However, Daddi et al. (2005b) find that the (Chary & Elbaz 2001) IR model template with $L_{IR} = 10^{12.2}$ $L_\odot$ fits the average SED of 24 μm–detected BzK objects at $\langle z \rangle = 1.9$, suggesting that the uncertainty in the templates is not severe. Nevertheless, we add 0.3 dex as a systematic error on the inferred L_{IR} to account for the systematic scatter in this conversion.

The uncertainty of the photometric redshifts leads to another source of uncertainty in the conversion from $L_\nu(24\mu m/[1+z])$ to the total IR luminosity. Owing to the large bolometric corrections from the mid–IR to the total IR luminosities, small changes in the redshift have a significant effect (see Papovich & Bell 2002). We find that taking the 68% confidence range on the photometric redshifts of the DRGs leads to variations in the inferred L_{IR} of 0.4 dex. We add this source of error in quadrature with the uncertainty from the IR templates, bringing the total error budget on the derived IR luminosities to 0.5 dex.

Figure 4 shows the total IR luminosities of the DRGs. The completeness limit (converted to a total IR luminosity in the same way as for the 24 μm detected galaxies) is indicated in Figure 4 as the solid line. The figure also shows the total IR luminosity for the HDF–N galaxies in this redshift range derived from deeper 24 μm observations (see § 2.4). The total IR luminosities of the 24 μm–detected DRGs are 10^{11-14} $L_\odot$, or $10^{11-13.5}$ $L_\odot$ if we exclude X–ray detected sources. The majority of these objects have IR luminosities comparable to local ULIRGs, $L_{IR} \gtrsim 10^{12}$ $L_\odot$, which if attributed to star–formation implies SFRs greater than 100 $\mathcal{M}_\odot$ yr^{-1}.

Several of the DRGs (6/152) have IR luminosities, $L_{IR} \geq 10^{13}$ $L_\odot$ (so–called Hyper luminous IR galaxies, HyLIRGs). These IR luminosities are comparable to those of PG quasars
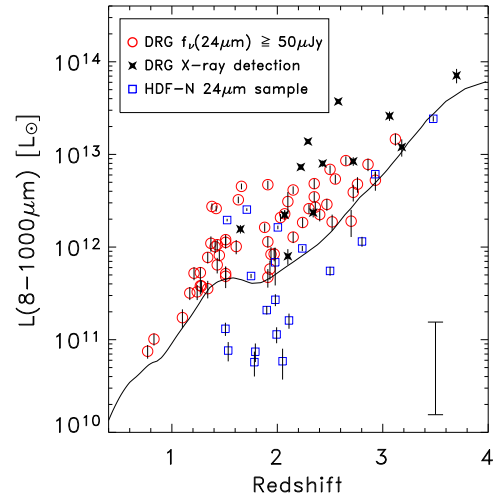

FIG. 4.— Total IR luminosities, $L_{IR} \equiv L(8-1000\mu m)$, of galaxies inferred from their observed MIPS 24 μm emission. Red circles show the IR luminosities for the GOOD–S DRGs detected at 24 μm, black stars show DRGs with both X–ray and 24 μm detections, and blue squares show objects detected by MIPS 24 μm in the HDF–N. The solid line denotes the 50% completeness limit of the GTO 24 μm data in the CDF–S, $f_\nu(24\mu m) = 60$ μJy. Error bars include only uncertainties on the 24 μm flux density. We estimate that the systematic uncertainties on the conversion between $f_\nu(24\mu m)$ and $L(8-1000\mu m)$ are typically ≈ 0.5 dex (inset, and see text).

at $z \gtrsim 1$, which have warm thermal dust temperatures (Haas et al. 2003). Locally, HyLIRGs — and many ULIRGs with $L_{IR} \geq 10^{12.3}$ $L_\odot$ have rest–frame optical emission spectra characteristic of Seyfert galaxies (e.g. Soifer et al. 1995; Veilleux et al. 1995; Sanders & Mirabel 1996; Veilleux et al. 1999), and the IR emission possibly originates from AGN processes. We suspect that the most IR–luminous DRGs may have a contribution to their bolometric emission from AGN. The majority (5/6) of the DRGs with inferred $L_{IR} \geq 10^{13}$ $L_\odot$ are detected by *Chandra*, compared to the 10% X–ray–detection fraction over the whole sample. This X–ray detection fraction is consistent with the limit on the AGN fraction for the coeval sub–mm galaxies (Alexander et al. 2005), a source population that also has inferred $L_{IR} \sim 10^{13}$ $L_\odot$. HyLIRGs are also present in high–redshift IRAC–selected AGN samples, and $\sim 50\%$ are undetected in deep X–ray data (Alonso–Herrero et al. 2005). Therefore, the X–ray emission from AGN in many of these IR–luminous objects may be attenuated by dust below the detection limit of the surveys. However, if AGN contribute to the emission in DRGs with $L_{IR} \gtrsim 10^{13}$ $L_\odot$, then we may be overestimating the galaxies' IR luminosity. Although the Dale & Helou (2002) IR templates include galaxies with $L_{IR} \gtrsim 10^{13}$ $L_\odot$, using a template for Mrk 231 with a known AGN and warmer dust temperature would reduce the inferred IR luminosity by factors of $\sim 2-3$. To limit the effects of any bias caused by IR template uncertainties for the highest luminosity DRGs, we consider below how restricting our sample to galaxies without X–ray detections, $L_{IR} \leq 10^{13}$ $L_\odot$, and IR colors indicative of AGN (see § 6.3) affects our analysis.

4.2. *The Relation Between the UV Spectral Slope and the Infrared Excess*

Locally, UV–selected starburst galaxies have a relation between their UV spectral slope, β, where $f_\lambda \sim \lambda^\beta$, and the

ratio of their IR to UV luminosity (also termed the "infrared excess"; e.g., Meurer et al. 1999). This relation links an observed increase in β with greater dust extinction of the intrinsic spectrum of a young stellar population. The dust–absorbed UV light is radiated in the thermal infrared, yielding an anti-correlation between the UV and IR. While this relation holds for a range of UV–luminous starburst galaxies (Meurer et al. 1999), it does not apply to other types of star–forming galaxies, including normal galaxies (Kong et al. 2004; Buat et al. 2005), and ULIRGs (Goldader et al. 2002), apparently due to geometry effects between the UV and IR emitting regions. Using the IR luminosities from § 4.1, we test whether the local relation between the UV spectral slope and the IR excess applies to the DRGs. We also test if it applies to other high–redshift galaxies detected by MIPS at 24 μm.

Following Meurer et al. (1999), we calibrated measurements of β by comparing the UV spectral slope derived from the full UV SEDs of local starburst galaxies, $\beta_{\rm spec}$, with that measured using only a broad–band photometric color, $\beta_{\rm phot}$. The correction for the difference between $\beta_{\rm spec}$ and $\beta_{\rm phot}$ is necessary as starburst–galaxy spectra contain numerous absorption and emission features. A spectroscopic UV slope is fit to spectral windows to avoid these features (Calzetti et al. 1994), but they are unavoidable in measuring β from broad–band colors. We fit the spectral slope, $\beta_{\rm spec}$, using the UV SEDs of starburst galaxy templates (Kinney et al. 1996), which have dust extinction varying from $E(B-V) < 0.10$ to $0.61 < E(B-V) < 0.70$. We then shifted these spectra to the observed frame at $z = 0.5-4$, and measured the observed ACS $B_{435} - V_{606}$, $B_{435} - i_{775}$, $V_{606} - i_{775}$, and WFPC2 $V_{606} - I_{814}$ colors. We measured the approximate UV spectral slope from the ACS and WFPC2 broadband photometry, $\beta_{\rm phot}$, using the effective wavelengths of the filters, $\beta_{\rm phot} = 3.20(V_{606} - I_{814}) - 2.0$ for the WFPC2 bands, and $\beta_{\rm phot} = 2.91(B_{435} - V_{606}) - 2.0$, $\beta_{\rm phot} = 1.59(B_{435} - i_{775}) - 2.0$, and $\beta_{\rm phot} = 2.14(V_{606} - z_{850}) - 2.0$ for the ACS bands. We then fit a quadratic polynomial to the difference, $\beta_{\rm spec} - \beta_{\rm phot}$, as a function of redshift.

To derive the UV spectral slopes of the DRGs, we want to span the longest wavelength baseline in the rest–frame wavelength range 1250–2800 Å. At wavelengths longer than 2800 Å there may be a significant contribution to the SED from A– and later–type stars from previous star–formation episodes (e.g., Calzetti et al. 1994). Therefore, for galaxies at $z > 2.2$ in the GOODS–S field, we will use the $V_{606} - z_{850}$ color to measure β. For galaxies with $1.7 \leq z \leq 2.2$, we will instead use the $B_{435} - i_{775}$, where the lower redshift bound results from the fact that below this redshift the i_{775}–band probes $\lambda > 2800$ Å. For galaxies with $1.2 \leq z < 1.7$, we use $B_{435} - V_{606}$ to derive the UV spectral slope. For $z < 1.2$, there are no ACS colors that measure the UV spectral slope at $\lambda < 2800$ Å.

For galaxies from the HDF–N with WFPC2 photometry and redshift, z, we derive the UV spectral slope, β, using the quadratic fit to the empirical relationship (cf., Meurer et al. 1999),

$$\beta = 3.20(V_{606} - I_{814}) - 4.45 + 2.03z - 0.423z^2. \quad (1)$$

For the DRGs with ACS photometry we use

$$\beta = \begin{cases} 2.91(B_{435} - V_{606}) - 3.35 + 1.49z - 0.438z^2, & 1.2 \leq z < 1.7 \\ 1.59(B_{435} - i_{775}) - 3.92 + 1.97z - 0.512z^2, & 1.7 \leq z \leq 2.2 \\ 2.14(V_{606} - z_{850}) - 4.76 + 2.14z - 0.418z^2, & z > 2.2. \end{cases}$$
$$(2)$$

We find that the different formulae give consistent results within the photometric errors for galaxies in redshift intervals where several ACS colors can be used to measure β. Using these formulae, we then calculate the UV spectral slopes of the DRGs and HDF–N galaxies using the appropriate ACS and WFPC2 bands, respectively. We also use uncertainties of the observed colors and the covariant uncertainties of the polynomial fits to estimate the error in β.

Figure 5 shows the relation between β and the IR/UV luminosity ratio for the high–redshift galaxies, and compares them to the local relation from Meurer et al. (1999). Many of the HDF–N 24 μm–detected galaxies at $1.5 < z < 3.5$ have UV spectral slopes and IR/UV luminosity ratios that lie near the local relation. These systems have IR luminosities in the range $L_{\rm IR} \sim 10^{10-11} L_\odot$, comparable to the IR luminosities in the Meurer et al. sample. There is a trend for galaxies with higher IR/UV luminosity ratios to move away from the local relation in the sense that they have more IR luminosity than otherwise predicted from their UV luminosity and spectral slopes.

This trend in galaxies with higher IR luminosities having higher UV/IR ratios is continued for the 24 μm–detected DRGs. The DRGs span $\beta \sim -2$ to 2 (with the exception of one object with $\beta \simeq 3.7$ and large photometric uncertainty). Many of DRGs with $L_{\rm IR} \leq 10^{12} L_{\rm IR}$ and some with $L_{\rm IR} > 10^{12} L_\odot$ have IR/UV ratios near the Meurer et al. relation. However, most of the DRGs have IR/UV luminosity ratios of more than one order of magnitude in excess of what would be predicted from their spectral slopes. That is, the total amount of star formation in these galaxies will be underestimated from their UV rest–frame luminosities and spectral slopes alone. This result is qualitatively unchanged if we restrict the DRG sample to redshifts $1.5 < z < 2.5$, where the total correction factor from observed $f_\nu(24\mu{\rm m})$ to $L_{\rm IR}$ spans a relatively narrow range compared to that for the full sample.

The DRGs occupy a very similar range of β and IR/UV flux ratios as has been observed for local ULIRGs (Goldader et al. 2002). In local ULIRGs the geometry of the forming star clusters and dust is highly complex. The UV and IR emitting regions are typically displaced from one another, or "patchy", such that the regions that dominate the UV emission are unassociated with the regions producing the large IR luminosity (as is the case for local IR–luminous galaxies with *ISO* IR and *HST* UV imaging; see Charmandaris et al. 2004). A similar situation probably holds for the 24 μm–detected DRG population. It is also plausible that the galaxies with the largest IR luminosities have more complicated geometries to account for the fact that these galaxies have the largest offsets from the local relation. Charmandaris et al. noted that for many of the local LIRGs, the *ISO* source is offset from the regions that dominate the UV emission by as much as several kpc, and such objects can have large IR excesses. This effect should be even stronger for ULIRGs. At redshifts typical of the DRGs, this corresponds to less than $1''$, and will be unresolvable with MIPS at 24 μm.

Most of the X–ray–detected DRGs have IR/UV luminosity ratios and UV spectral slopes comparable to the rest of the DRG sample, although several have the most extreme IR/UV luminosity ratios or UV spectral slopes ($\log L_{\rm IR}/L[1600{\rm Å}] \sim 4$, and/or $\beta \sim -2$), lying away from the other DRGs. We suspect that an AGN contributes substantially to the IR emission, the UV emission, or both. In this case, the Dale & Helou (2002) IR templates may overestimate the IR luminosity in
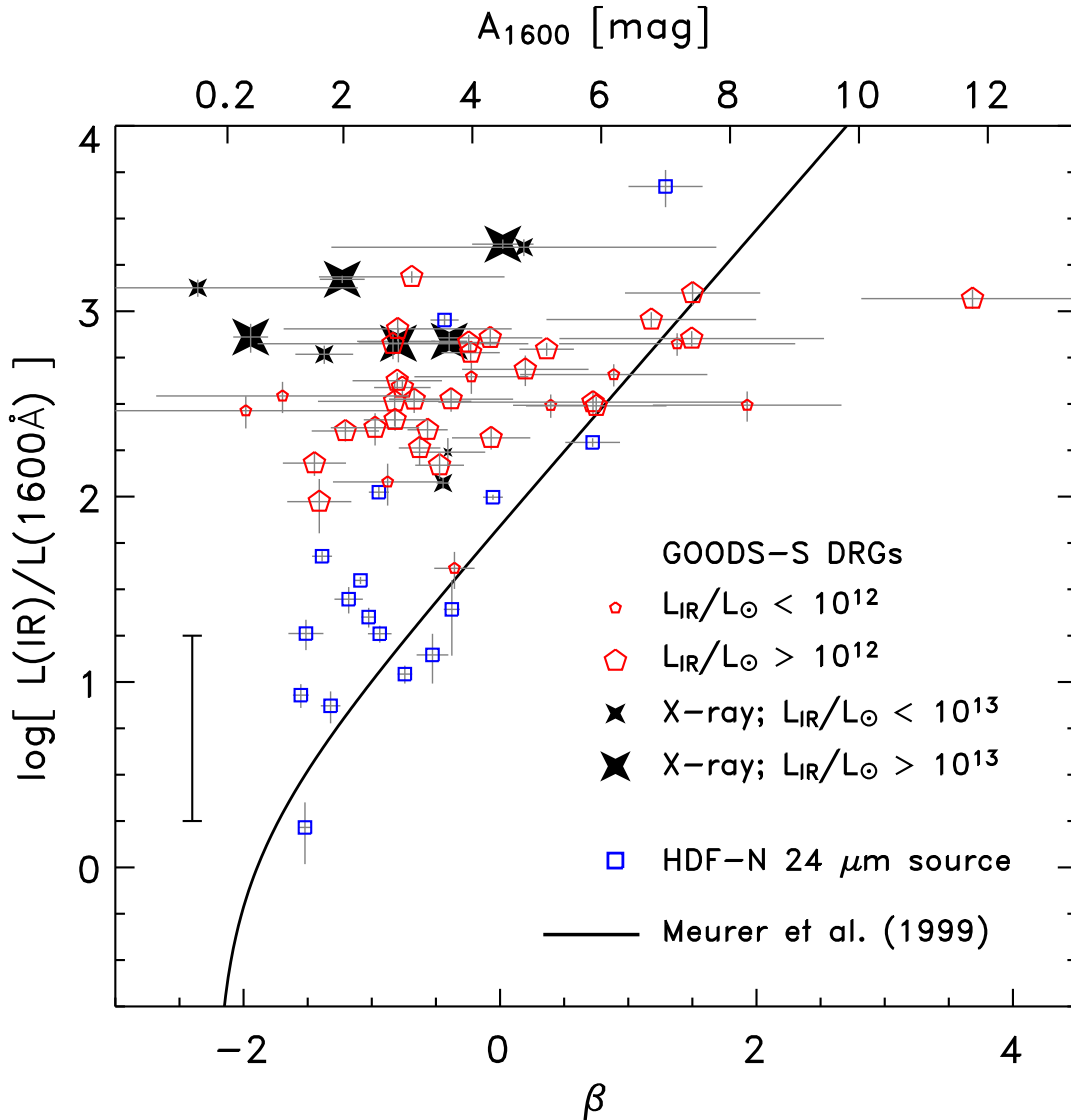
FIG. 5.— Relation between the IR/UV luminosity ratio and the UV spectral slope, β, where $f_\lambda \sim \lambda^\beta$. The solid line shows the relationship for local UV–luminous starburst galaxies from Meurer et al. (1999). Red pentagons denote the GOODS–S DRGs, black stars indicate DRGs with X-ray detections, and the symbol size scales with IR luminosity (see plot inset). Blue squares denote galaxies with 24 μm detections from the HDF–N. The top abscissa shows the extinction at 1600 Å that corresponds to β (see Meurer et al. 1999). Error bars on the IR/UV luminosity ratios only correspond to the uncertainties on flux density measurements. The systematic uncertainty in the conversion between $f_\nu(24\mu m)$ and L_{IR} is ≈ 0.5 dex, and is indicated by the inset error bar.

these objects (see § 4.1).

4.3. Inferring the Star Formation Rates of High–Redshift Galaxies from Bolometric Luminosities

Nearly all of the bolometric luminosity from star–forming regions is emitted in the UV and IR (e.g., Bell 2003). Therefore, we estimate the instantaneous star–formation rates (SFRs) for galaxies in our samples using the combination of their UV and IR luminosities.

We use the SFR conversion from Bell et al. (2005a), based on the UV and IR calibration presented by Kennicutt (1998),

$$\Psi/\mathcal{M}_\odot \ \mathrm{yr}^{-1} = 1.8 \times 10^{-10} \times (L_{IR} + 3.3 \, L_{2800})/L_\odot, \qquad (3)$$

where L_{IR} is the total IR luminosity, and $L_{2800} \equiv \nu L_\nu(2800\text{Å})$ is the monochromatic luminosity at rest–frame 2800 Å interpolated from the ACS photometry. We have adjusted the SFR

to correspond to a single power–law, Salpeter IMF with mass cutoffs of 0.1 and 100 $\mathcal{M}_\odot$. Bell (2003) tested these UV+IR–derived SFRs against extinction–corrected Hα and radio–derived measures, finding excellent agreement with $\lesssim 0.3$ dex scatter and no offset. Nevertheless, it should be noted that the UV and IR–calibrations are based on local galaxy correlations. Although the indications are these hold at higher red-shifts (see, e.g., Elbaz et al. 2002; Appleton et al. 2004), they should be used with some caution.

This calibration explicitly assumes that star–formation processes account for the bolometric UV and IR emission. However, the presence of AGN may also contribute some (or all) of this bolometric emission from accretion processes onto supermassive black holes (SMBHs). Therefore, the SFRs derived using equation 3 may be upper limits if AGN are present (modulo uncertainties in the conversion from the 24 μm to IR
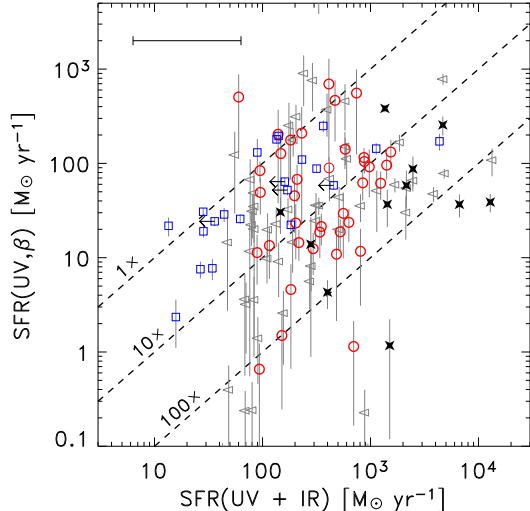
FIG. 6.— Comparison between the SFRs derived from the extinction–corrected UV luminosity and the SFRs derived from the sum of the UV and IR luminosities as described in the text. Red circles denote DRGs detected at 24 μm, and gray triangles show upper limits for DRGs with undetected at 24 μm. Black stars indicate DRGs detected in X–rays. Blue squares denote galaxies from the HDF–N at $1.5 \leq z \leq 3.5$. Error bars on the UV + IR–derived SFR are ≈ 0.5 dex, as indicated by the inset error bar. The diagonal lines indicate constant ratios of 1, 10, and 100, as labeled.

luminosity).

Figure 6 compares the SFRs derived from the sum of the UV and IR emission using equation 3 versus those derived using solely the UV rest–frame luminosity corrected for extinction using the derived spectral slopes (see e.g., Meurer et al. 1999; Adelberger & Steidel 2000). To calibrate the UV–derived SFRs, we compared the 1600 Å luminosity (averaged over the range 1400–1800 Å) to the SFR from Bruzual & Charlot (2003) spectral templates over a wide variety of star–formation histories. For a single power–law Salpeter IMF with mass limits 0.1 and 100 $\mathcal{M}_\odot$, we find that a SFR of 1 $\mathcal{M}_\odot$ yr^{-1} corresponds to a luminosity density of $l_\nu(1600\text{Å}) = 8.7 \times 10^{27}$ erg s^{-1} Hz^{-1} for galaxies with ongoing star formation for $\gtrsim 10$ Myr (see, e.g., Madau et al. 1998). Figure 6 shows this relation for the GOODS–S DRGs, and the HDF–N galaxies. The HDF–N galaxies extend to smaller SFRs, which are in closer agreement with the rest–frame UV data. The DRGs and many of the HDF–N galaxies with larger IR luminosities have significantly larger SFRs derived from the UV+IR than those estimated from the UV only. The difference can be up to two orders of magnitude.

5. STELLAR POPULATIONS AND STAR FORMATION IN HIGH REDSHIFT GALAXIES

In § 3, we showed that the UV, optical, and near–IR colors of $J - K_s$–selected galaxies are consistent with a multi–variate population of heavily dust–enshrouded starbursts and galaxies whose rest–frame optical and near–IR light are dominated by later–type stars. Here, we extend this analysis by comparing the full photometry of the DRG and HDF–N samples to stellar population synthesis models. As in Papovich, Dickinson, & Ferguson (2001), we first consider a model of a single, monotonically evolving stellar population with a SFR that decays exponentially with a characteristic e–folding timescale, τ. In reality, the star–formation his-

tories of high–redshift galaxies are presumably more complex, involving stochastic events from mergers, interactions, feedback from star formation and AGN, as well as quiescent star formation (e.g., Somerville, Primack, & Faber 2001; Nagamine et al. 2005; De Lucia et al. 2005). The models here should be considered as fiducial averages of past star–formation histories. Our definition of galaxy "age" is the time since the onset of star formation. Our monotonically evolving models continuously produce new stars with young ages (albeit at a lower rate than in the past). For example, under our definition a stellar population formed with a constant SFR has age, t, while the mean age would be $\int \Psi(t) t \, dt / \int \Psi(t) \, dt = t/2$, and the luminosity–weighted mean age (weighted heavily toward the short–lived early–type stars) would be younger still. The definition of galaxy age also neglects all previous discrete, episodes of star–formation. Older stellar populations from past star–forming events may very well exist, but be lost in the "glare" of the nascent stars. We consider these effects by using a second model that adds a maximally old stellar population formed in a single burst at $z = \infty$ to the stellar populations formed with the simple exponentially decaying models described above (see also, Papovich, Dickinson, & Ferguson 2001; Dickinson et al. 2003). The latter model has a maximal stellar-mass–to–light ratio. We will use the single–component and two–component models to constrain the range of stellar masses and star–formation histories.

5.1. Fitting the Models to the Photometry

We fit the galaxy photometry with the Bruzual & Charlot (2003) stellar–population synthesis models. While the metallicities of the DRGs are poorly known (Förster–Schreiber et al. 2004), van Dokkum et al. (2004) provide evidence for solar and super–solar metallicities for luminous DRGs. Shapley et al. (2004, 2005) have estimated the metallicities of massive ($\mathcal{M} \gtrsim 10^{11}$ $\mathcal{M}_\odot$) U_n–dropout–selected LBGs at similar redshifts to be approximately solar. Because the expected colors for the majority of massive U_n–dropouts satisfy the DRG selection criteria (Reddy et al. 2005; Shapley et al. 2005), the solar–metallicity assumption for DRGs is also reasonable. Using different metallicities will affect our fitting results. However, the derived stellar masses vary by factors of less than 2–3 (Papovich, Dickinson, & Ferguson 2001).

We use models with a single power–law Salpeter IMF with mass limits 0.1 and 100 $\mathcal{M}_\odot$. Changing the shape of the IMF affects the derived stellar masses (and other stellar population parameters as well; see Papovich et al. 2001). For example, the Chabrier, Kennicutt, or Kroupa IMFs have a turnover in the mass function below 1 solar mass and produce stellar populations with roughly the same colors but with a stellar mass of 0.25 dex lower than that for the adopted Salpeter IMF. Although these other IMFs possibly better reflect nature, we choose to use a Salpeter IMF to facilitate comparisons of our results with those in the literature. As of yet there is no reason to expect the IMF to differ strongly from that observed in local galaxies (e.g. Baldry & Glazebrook 2003; Larson 2005), although some empirical studies and theoretical predictions suggest a steeper IMF may be required in high–redshift massive starbursts (Ferguson et al. 2002; Baugh et al. 2005).

We generate a suite of photometry from the Bruzual & Charlot (2003) models for galaxies spanning the range of redshifts in our sample with a redshift step–size of $\delta z = 0.05$. The models range in stellar population
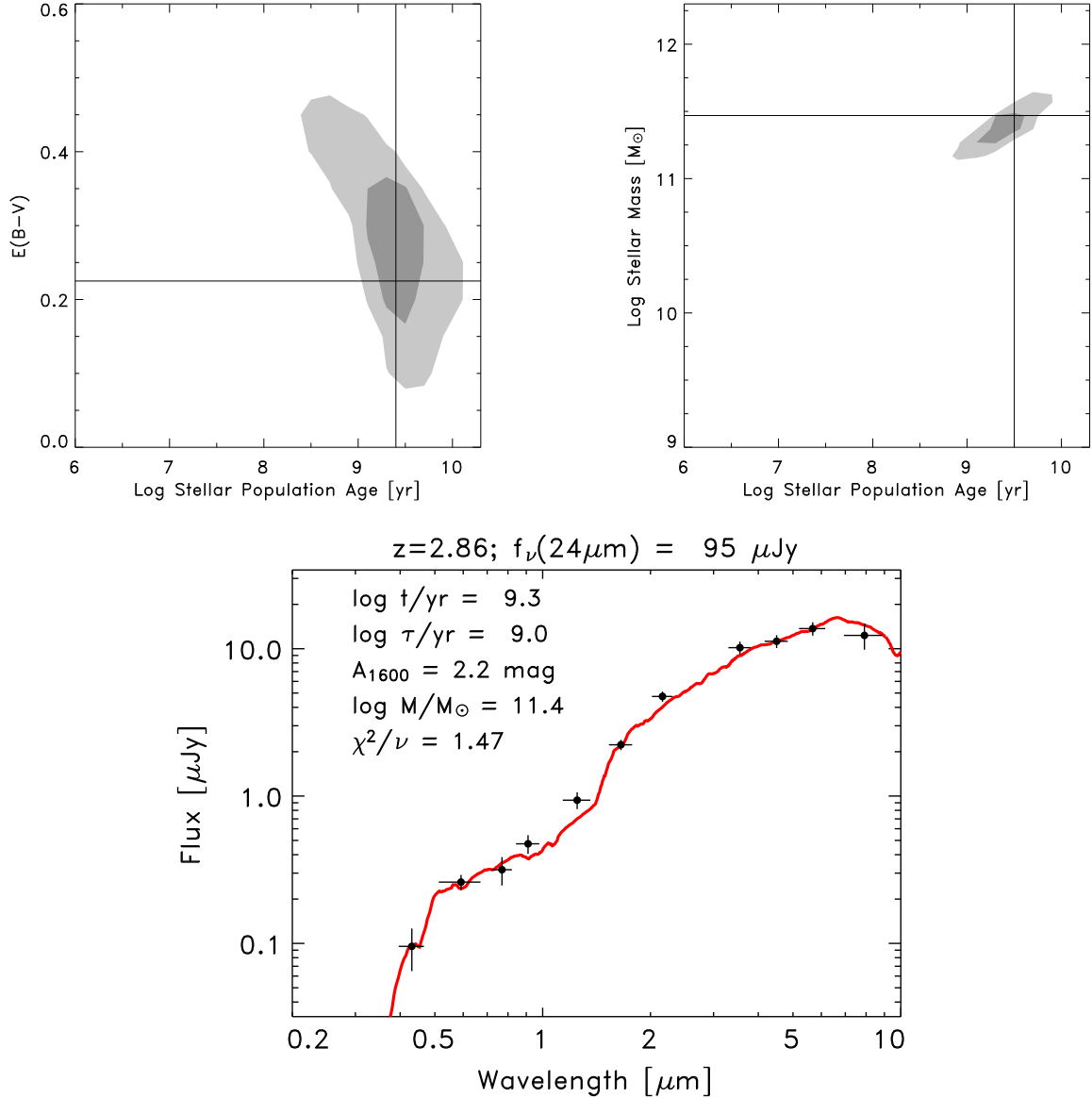
FIG. 7.— Illustration of spectral synthesis model fitting results for one of the GOODS–S DRGs which has an indication of both young and old stellar populations. The star formation history used here is parameterized as a monotonic, decaying exponential with e–folding time τ, as described in the text. The top panels show the 68 and 95% confidence intervals on various quantities plotted against the stellar population age: dust extinction (parameterized as the color excess, $E[B-V]$), and the stellar mass. The cross hairs show the most–likely parameter values in each two–dimensional projection of the full probability distribution function. The bottom panel shows the best–fit model spectrum in the observed frame, and the best–fit set of parameters for this galaxy. The data points show the ACS $B_{435}V_{606}i_{775}z_{850}$, ISAAC JHK_s, and IRAC 3.6–8.0 μm photometry and errors.

age from 10^6 to 2×10^{10} yr in the quasi–logarithmic steps provided in the models. We include dust extinction using the Calzetti et al. (2000) law with color–excess values $E(B-V) = 0.0 - 0.6$ in steps of $\delta E(B-V) = 0.025$. For the Calzetti et al. extinction parameterization, these color excesses correspond to extinctions in the UV (rest–frame 1600 Å) of $A_{1600} = 0 - 6$ mag in increments of $\delta A_{1600} = 0.25$ mag. We make the assumption that in these high–redshift galaxies the Calzetti et al. extinction law applies to the stellar populations dominating the light observed in the ACS, ISAAC, and IRAC passbands (although it may not apply to the ionizing source responsible for the far–IR emission, see § 4.2). Using different extinction laws would

affect the derived stellar–population ages and extinction, but would not strongly change the inferred stellar masses (Papovich, Dickinson, & Ferguson 2001). We also make the assumption that the stellar populations dominating the rest–frame UV to near–IR also dominate the stellar mass. If a substantial fraction of the galaxies' stellar mass is obscured from view, then the stellar–mass derived from the SED modeling will be underestimated. We first allow for a range of star–formation histories with a SFR parameterized as a decaying exponential with a e–folding time, τ, where the SFR at any age, t, is given by $\Psi(t) \sim \exp(-t/\tau)$. In our models, τ ranges from 1 Myr to 100 Gyr in quasi–logarithmic steps. Short–duration τ values correspond to instantaneous bursts of star formation while long–duration τ values correspond
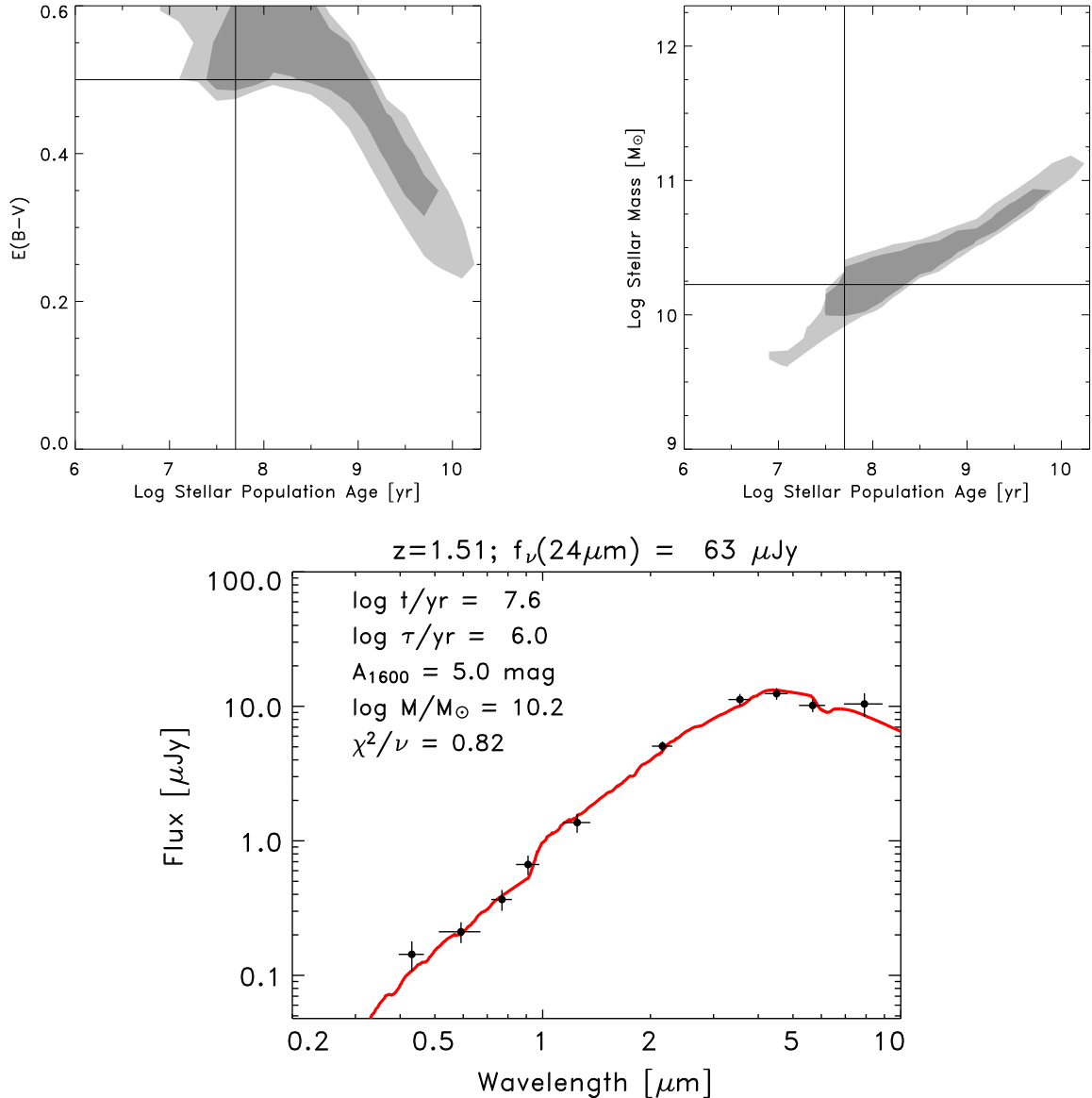
FIG. 8.— Same as Figure 7, but for one of the DRGs with a near–power-law-like rest–frame UV–to–near–IR SED. The best–fitting models generally prefer a SED that is dominated by young stars and heavily extincted by dust.

approximately to constant star–formation histories.

For each DRG, we fit all available bands among the ACS $B_{435}V_{606}i_{775}z_{850}$, ISAAC JHK_s, and IRAC [3.6µm] and [4.5µm] data. In the model fitting, we add a $\sigma/f_\nu = 4\%$ error in quadrature to the photometric uncertainties on each band to account for the fact that the population–synthesis models do not continuously sample the model parameter space (see Papovich, Dickinson, & Ferguson 2001). The fits provide a normalization between the photometry and the model, and a minimum χ^2 for each particular model with a distinct set of parameters. The IRAC [5.8µm] or [8.0µm] photometry because the longer–wavelength IRAC data generally have lower signal–to–noise ratios, and it is possible that at rest–frame $\gtrsim 2$ µm PAH features or emission from obscured AGN shift into the IRAC bandpasses. Some galaxy SEDs show evidence for such features in these data (see Figure 2), and so we exclude these points to avoid any potential bias. However, we

find that a majority of the best–fit models broadly reproduce the [5.8µm] and [8.0µm] photometry, which lends credence to the fits.

The model with the minimum chi–squared value, χ^2_0, is the model with the best–fit for a given set of parameters (t, τ, $E[B-V]$, and $\mathcal{M}$; the latter is derived using the stellar–mass–to–light ratio of the model, see Papovich et al. 2001). Using the $\Delta\chi^2$ difference between the chi–squared value derived for other models with a different set of parameters and χ^2_0, we can construct confidence regions on each parameter in the model. For each galaxy we generated up to 1000 Monte Carlo realizations for the photometry by perturbing the measured flux densities by a random value taken from a Normal distribution with a standard deviation equal to the flux–density errors. We then refit the new photometry and re-obtain best fits on all model parameters. We do not take into account errors in the photometric redshifts, which can affect the derived star–

formation histories but generally have little effect on the inferred stellar masses (see Dickinson et al. 2003). We identify the $\Delta\chi^2$ values from the fit to the measured data that encompasses 68% and 95% of the best–fit values from the Monte Carlo realizations, which provides the equivalent confidence range on the model parameters for each source.

5.2. *Stellar population models with single exponentially decaying star–formation histories*

Figures 7 and 8 present examples of the results for two of the DRGs using the single–component star–formation history models. The examples are typical of the two populations identified by the $(J-K_s)_{\rm Vega} > 2.3$ mag selection. Each figure shows the probability distribution function in two–dimensional projections of the age–extinction, and age–mass planes. The figures also show the best–fit model spectrum over all parameters (i.e., the model with the minimum χ^2 from all models) overplotted on the data.

Figure 7 shows a galaxy with a strong 4000 Å/Balmer break between the J– and K_s–bands presumably due to a substantial mature stellar population. The galaxy also has a small amount of ongoing star–formation that produces the rest–frame UV light. The best–fit model corresponds to a star–formation history that has undergone roughly $t/\tau \simeq 2$ e–folding times. For this model, the galaxy formed most of its stellar mass in the past at a substantially higher SFR. The early–type (OB type) stars from the early onset of star formation have died off, and thus most of the stellar mass resides in later–type stars, which formed well in the past and now dominate the optical and near–IR rest–frame light. The best–fit model requires substantial dust extinction: > 2 mag at 1600 Å (68% confidence). The estimated stellar mass is quite robust for this set of star–formation histories. The 68% confidence range on the stellar mass ranges from $1.6-2.7 \times 10^{11}$ $\mathcal{M}_\odot$, with a most–likely value of 2.4×10^{11} $\mathcal{M}_\odot$.

Figure 8 shows a galaxy with a heavily extincted recent starburst. The best–fit model to this galaxy is a young stellar population formed roughly instantaneously in a burst 40 Myr in the past. However, the 68% confidence range on the stellar–population age ranges from ~ 30 Myr to several Gyr. For all possible ages, the modeled star–formation history has undergone many e–folding times and has substantial dust extinction, which is required to produce the red UV–to–near-IR rest–frame colors. This best–fit model requires 5 mag of extinction at 1600 Å. Owing primarily to the larger model degeneracies in the age and dust extinction for this galaxy, the stellar mass is less well constrained compared to the example in Figure 7. The 68% confidence region on the stellar mass is 9×10^9 to 8.4×10^{10} $\mathcal{M}_\odot$, with a most–likely value of 1.6×10^{10} $\mathcal{M}_\odot$.

5.3. *Stellar population models with double component star–formation histories*

We also fit the DRG photometry models with a two–component star–formation history characterized by a passively evolving stellar population formed in a previous "burst" with $z_{\rm form} = \infty$, summed with the exponentially–decaying–SFR model above. For these models, the stellar–population age is the time since the onset of star formation in the monotonically evolving component. These models check the effects of discrete bursts on the derived parameters. Our choice of a burst at $z_{\rm form} = \infty$ is a proxy for bursts at all times before the observed redshift, and reducing $z_{\rm form}$ would not strongly

affect our conclusions. Placing the burst at $z_{\rm form} = \infty$ provides a limit on the maximum stellar mass because it has the maximal mass–to–light ratio possible at the observed redshift.

Figure 9 shows the results for the two–component model fits to the two DRGs described above. For the galaxy shown in Figure 7, a very young ($t \sim 10$ Myr), heavily extincted ($A_{1600} \sim 3$ mag) starburst dominates the UV rest–frame emission. The optical and near–IR rest–frame emission is produced by the previously formed population, which is now quite old. However, the 68% confidence range on the age and dust extinction shows that a large region of the parameter space fits the data equally well. This is in contrast to the region permitted by the single–component model fits in Figure 7. Clearly the interpretation of the ages and extinction depend strongly on the assumed star–formation history. However, the derived stellar masses are fairly robust. The total stellar mass is nearly unchanged in this model relative to the single–component model above; the 68% confidence range is $1.6-2.3 \times 10^{11}$ $\mathcal{M}_\odot$. The upper range of the confidence region drops simply because in the previous model we did not enforce the constraint that the age of the model be less than the age of the Universe at the given redshift. Such a constraint is imposed (by construction) on the two–component fits, and as a result there is less time for stellar populations to evolve, produce large mass–to–light ratios, and increase the stellar mass.

The best–fit two–component star–formation history model for the galaxy in Figure 8 shows little change compared to the single–component fit. In this case, young, reddened stars dominate the light at most wavelengths for both types of models. Thus, for galaxies of this sort, adding the second component only provides an upper limit on the inferred stellar mass content.

In general, the two–component fits for the DRGs appear more consistent with the data than the less complex, single–component models. Figure 10 compares the reduced χ_0^2 from the fits to the single–component models to the reduced χ_0^2 from the fits to the two–component models for all the DRGs. For many DRGs (91/152), adding the second model component to the fit has little effect on the minimum reduced χ^2, and these points lie near the unity relation indicated in the plot. For a large fraction of DRGs adding the second burst lowers the reduced minimum χ^2 significantly. It is possible that some of this effect results from the fact that we have not included the contribution of emission lines in the various bandpasses. However, as noted earlier, this contribution should be small, contributing $\lesssim 0.1$ mag based on the observed emission–line equivalent widths (van Dokkum et al. 2004, 2005), except perhaps for galaxies with AGN, for which the models may not apply. Thus, in general this effect does not account for the smaller reduced χ^2 values observed in our galaxies. For example, the best–fitting single–component model for the galaxy in Figure 7 deviates from the J–band photometry at ~ 1 μm by nearly 2σ, whereas the two–component model is better able to reproduce this data point (see Figure 9).

The photometry in many of the DRGs is better represented by star–formation histories that are more complex than the simple, monotonically evolving exponentially decaying SFR. Formally, the χ^2 statistic rejects the single–component model for 13/152 DRGs at the 3σ level, while not rejecting the double–component model at this significance level. In contrast, the χ^2 statistic never rejects the double–component model in favor of the single–component model at this sig-
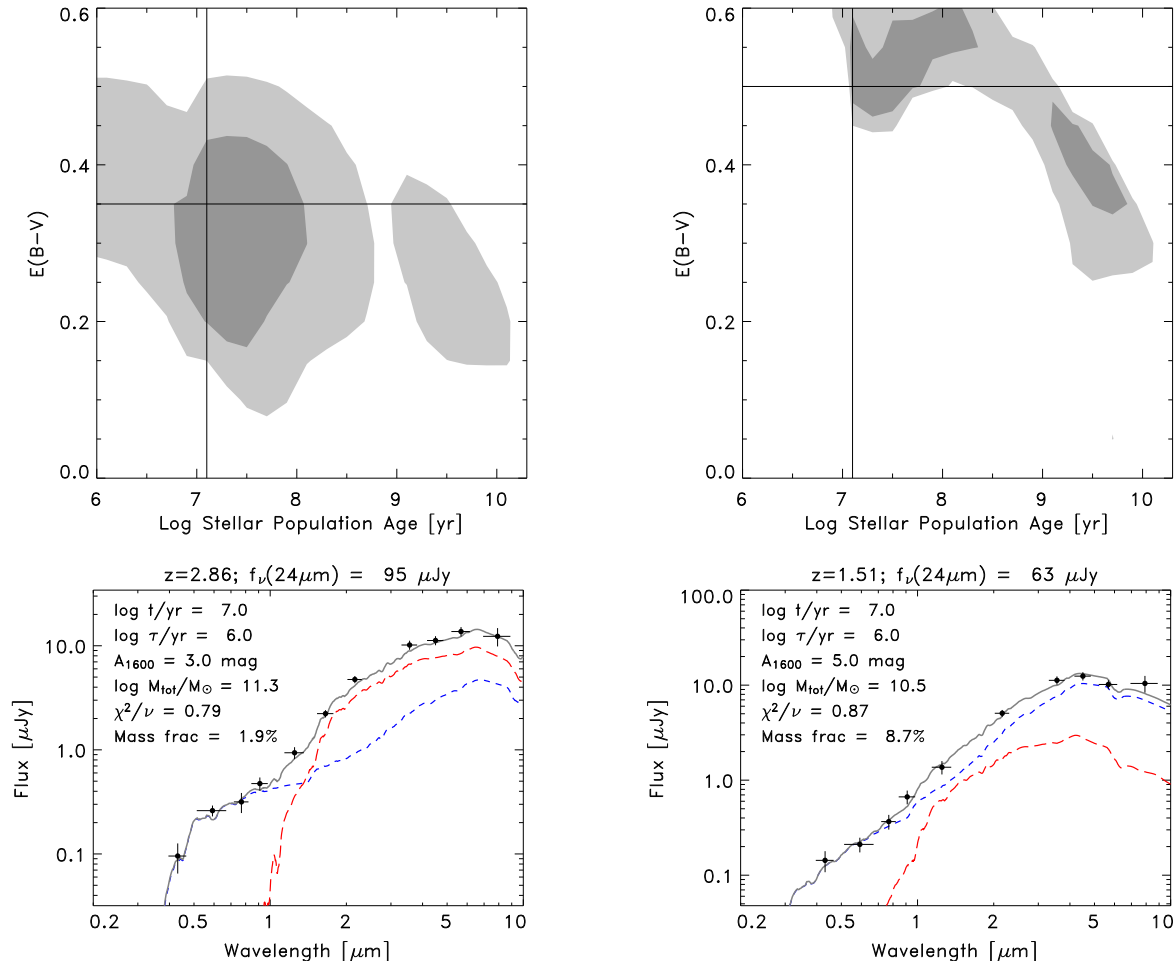
FIG. 9.— Best–fit stellar–population models with two components to the two example DRGs shown in Figure 7 and 8. The solid grey line shows the best–fitting two–component model, and the data points correspond to the observed photometry. The two galaxy components correspond to a monotonically evolving stellar population (blue, short–dashed line) and a stellar population formed in a single burst at $z = \infty$ (red, long–dashed line). The inset best–fitting parameters refer to the monotonically evolving stellar population. The mass fraction is the percent contribution of the younger, monotonically evolving stellar population to the total stellar mass. The top panels show the 68 and 95% confidence regions on the age and dust extinction parameters and correspond to the galaxy in the spectrum that lies below each plot. The cross hairs show the most likely value in the two–dimensional projection of the full probability distribution function.

nificance level. Furthermore, many of the best–fit single–component models favor stellar population ages that are older than the age of the Universe for the measured redshift (see § 6.1.2). Restricting these models to ages less than the age of the Universe increases the minimum χ^2 value, making the difference between single– and two–component fits more pronounced. We interpret this behavior to indicate that in general the DRG population has star–formation histories that are more complex than simple monotonically evolving stellar populations. A similar scenario has been suggested based on modeling the SEDs of LBGs at these redshifts (e.g., Sawicki & Yee 1998; Papovich, Dickinson, & Ferguson 2001; Papovich et al. 2004a; Shapley et al. 2005), and is likely consistent with hierarchical models (De Lucia et al. 2005; Nagamine et al. 2005).

6. DISCUSSION

The ensemble properties of the DRGs span a range of the stellar–population model parameter space. Broadly speaking, the $(J - K_s)_{\rm Vega} > 2.3$ mag color selection identifies galaxies whose rest–frame optical and near–IR light is dominated by

later–type stars, and galaxies whose light is dominated by heavily extincted starbursts (Franx et al. 2003). In this way, it is not dissimilar to traditional $R - K$ or $I - K$ selection criteria for EROs, but it tends to pick out objects at higher redshifts. In addition, roughly $\simeq 15\%$ of the DRGs are luminous in X–rays, implying that some of the UV to IR emission may stem from SMBH accretion processes rather than star formation. Here we consider the implications that our analysis has for star–formation in massive galaxies at high redshifts. We briefly consider AGN activity in these galaxies, with a more detailed analysis to be presented in L. A. Moustakas et al. (in preparation).

6.1. Stellar Populations and Star–Formation Histories of DRGs

6.1.1. Dust Extinction

The best–fitting single–component DRG models span extinctions of $\sim 0 - 6$ mag at 1600 Å. The mean dust extinction from the best fits to the ACS to IRAC photometry is $\langle A_{1600} \rangle = 3.1$ mag, with a standard deviation of 1.5 mag. The mean is substantially larger than that inferred

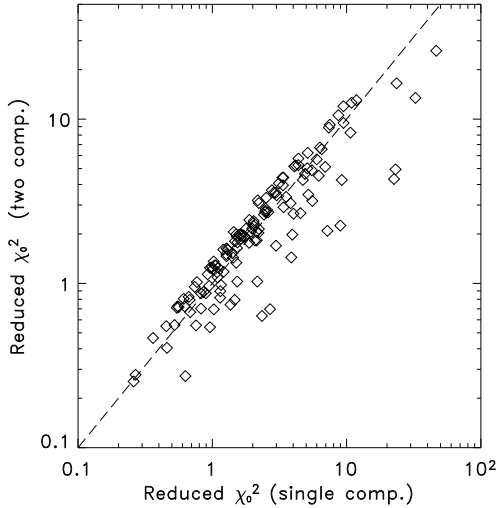FIG. 10.— Comparison of the minimum reduced χ^2 from fitting the DRGs with models of different star–formation histories. The abscissa shows the minimum reduced χ^2 derived for models with single–component, exponentially decaying star–formation histories. The ordinate shows the minimum reduced χ^2 for the two–component models where one component corresponds to the exponentially decaying star–formation histories and the other corresponds to an instantaneous burst of star–formation at $z_{\rm form} = \infty$, that evolves passively thereafter.

for UV–selected LBGs at comparable redshifts, for which Papovich, Dickinson, & Ferguson (2001) and Shapley et al. (2001) find average extinction values of 1.2 and 1.6 mag at 1600 Å, respectively. Förster–Schreiber et al. (2004) find that DRGs in the FIRES fields have median extinction of $\simeq 6.2$ mag at 1600 Å for the Calzetti extinction law (averaged by number), but restricted to models with constant SFR, and these values change little after including *Spitzer*/IRAC data (Labbé et al. 2005). Although on the surface this appears at odds with our findings, Förster–Schreiber et al. found that using exponentially declining models reduces the measured extinction by roughly a factor of two, in better agreement with our results.

To study differences between the sub–populations of DRGs (i.e., those with substantial mass in late–type stars and those dominated by highly dust–extincted starbursts), we divided the sample into subsets with $E(B-V) \leq 0.35$ and $E(B-V) > 0.35$. We have used the results from the fits to the single–component models for this selection, but there is little change if we use the two–component models. This division point is the approximate upper bound on values inferred for UV–selected LBGs (largely as a result of the UV–selection itself; e.g., Adelberger & Steidel 2000).

DRGs with $E(B-V) > 0.35$ comprise roughly 40% (61/152) of the full sample. These galaxies have a mean redshift of $\langle z \rangle \simeq 1.7$ with standard deviation $\sigma(z) = 0.5$. The mean dust extinction is 4.6 mag at 1600 Å for the Calzetti law. We estimate the resulting IR luminosities from these extinction values using the empirical relations between the UV luminosity, extinction, and far–IR luminosity (Meurer et al. 1999; Calzetti et al. 2000). In these galaxies, the observed UV luminosities and model extinction (using the 68% confidence limits) correspond to IR luminosities of $10^{11-12.5}\,L_\odot$. These are generally less than the 24 μm–derived IR luminosity or the 24 μm upper limit for undetected galaxies). However, because

the 68% confidence interval on galaxy extinction is large, $\delta A(1600) \sim 1-2$ mag, in roughly $\sim 50\%$ of the objects the extinction from the upper 68% confidence bound yields a $L_{\rm IR}$ comparable or exceeding the 24 μm value. This is consistent with the fraction of DRGs in figure 5 with IR/UV ratios and UV spectral slopes near the local relation from Meurer et al. (1999).

The DRGs with best–fit $E(B-V) \leq 0.35$ have a mean extinction of 2.0 mag at 1600 Å. Later–type stars dominate the rest–frame optical and near–IR light in these galaxies, while the UV rest–frame emission stems from small amounts (by mass) of ongoing star–formation with low to moderate extinction. The mean redshift for the DRGs with $E(B-V) \leq 0.35$ is $\langle z \rangle \simeq 2.5$, noticeably larger than that for the DRGs with higher extinction. This higher redshift range arises because galaxies with a strong Balmer/4000 Å break satisfy the $(J-K_s)_{\rm Vega} > 2.3$ mag selection only for $z \gtrsim 2.0$ as this break is moving through the J and H bands (Franx et al. 2003), whereas heavily reddened galaxies can enter the sample at lower redshifts. The lower $E(B-V)$ estimates from the model fitting would smaller IR luminosities relative to the DRGs with higher extinction described above. Unlike the case for the higher–extinction DRGs, the IR–luminosity for the the DRGs with $E(B-V) \leq 0.35$ are less than the 24 μm–derived $L_{\rm IR}$ by factors of $\approx 2-20$. Therefore, the observed 24 μm emission in DRGs with relatively low dust extinction from the SED modeling does not originate only from the extincted stellar populations that dominate the UV and optical rest–frame light. These galaxies require either additional embedded star formation, or an obscured AGN, or both, and these obscured components contribute negligibly at bluer wavelengths.

6.1.2. *Stellar Population Ages and Star Formation Histories*

Our stellar–population modeling of the DRGs is more sensitive to the ratio of model age, t, to the star–formation e–folding time, τ, than on t or τ individually, and we discuss them simultaneously. From the models with a single, exponentially decaying SFR the median age is 1.1 Gyr, and on average a DRG has undergone $t/\tau \simeq 4$ e–folding times. In an analysis of the 34 DRGs in the FIRES fields, Förster–Schreiber et al. (2004) tested constant star formation histories ($\tau \gg t$) and found median stellar population ages of $t \sim 1.7-2$ Gyr. The lower median ages for our models result because they favor star–formation histories with a smaller number of t/τ e–folding times than the constant star formation histories. Indeed, Förster–Schreiber et al. also considered models with $\tau = 300$ Myr, for which they derive a median age of 1 Gyr, implying $t/\tau \sim 3$. This is consistent with our result taken over a wider range of star–formation histories.

There are 17 DRGs ($\simeq 11\%$ of the sample) where the lower limits from the 68% confidence range from the single–component–model fits are older than the Universe. Of these, nine (53%) show indications of AGN activity either because they are detected in the *Chandra* data, they have $L_{\rm IR} > 10^{13}\,L_\odot$, and/or they have have IRAC colors satisfying the AGN selection of Stern et al. (2005, see also § 6.3). We suspect an AGN may influence the observed photometry and the model fits. The remaining DRGs have SEDs qualitatively similar to the example shown in Figure 7, but the model fits favor older ages. In all these cases the two–component model fits have solutions with ages less than the age of the Universe within the 68% confidence interval, and are thus more physical. Moreover the reduced minimum χ^2 values for the two–component fits are significantly improved for more than half

of these, implying such models are better realizations of the data.

Thus, including the constraint that the age of the model stellar population be less than that of the Universe favors models with more complicated star–formation histories than the single–component, monotonically evolving models. This reinforces our conclusion that the two–component models better describe the star–formation histories of the DRGs based on their lower reduced χ_0^2 values (see § 5.3). The real star–formation histories are probably even more complex. It is unlikely that the star–formation histories of DRGs are consistent with scenarios where all their mass formed in the distant past with subsequent passive evolution (see, e.g. Cimatti et al. 2002b). Massive galaxies at these redshifts continue forming stars up to the epoch we are observing them. Recent semi–analytic prescriptions of the star–formation histories of massive galaxies typically involve both stochastic "burst" modes, and quasi–continuous "quiescent" modes of star formation (e.g., Somerville, Primack, & Faber 2001; De Lucia et al. 2005; Nagamine et al. 2005), qualitatively consistent with our analysis. It seems that the earliest star–formation episodes in DRGs did occur in the distant past, and that much of their stellar mass was assembled much earlier than the epoch at which we are observing them. Taking the median age of the stellar population as a fiducial value for the onset of star formation, DRGs began forming stars at $z_{\rm form} \gtrsim 3.5$. Their progenitors may be the star–forming galaxies observed at those earlier epochs as UV–dropouts at $z \gtrsim 3.5$ (e.g., Papovich et al. 2004a).

6.1.3. *Stellar Masses*

The SED modeling provides relatively robust estimates of the stellar-mass-to–light ratios of these galaxies, providing good measures of their stellar masses. Figure 11 shows the distribution of the stellar masses for the single– and two–component star–formation histories for both the DRGs and the galaxies in the HDF–N. Typical errors are 0.1–0.3 dex (for a given IMF and metallicity).

The median stellar masses for the GOODS–S DRGs are 1.1 and $1.7 \times 10^{11} \, \mathcal{M}_\odot$ for the single– and two–component star–formation history models, respectively. There is little difference between the stellar masses of DRGs detected and undetected at 24 μm. The interquartile range (containing the inner 50% of the sample) spans from 0.13 to $3.3 \times 10^{11} \, \mathcal{M}_\odot$ for the single–component models, and from 0.29 to $4.6 \times 10^{11} \, \mathcal{M}_\odot$ for the two–component models. The main effect of the two–component models is to increase the masses of objects with low masses from the one–component models. Higher mass objects typically have larger stellar-mass–to–light ratios, $\mathcal{M}/L$, and are less effected because the uncertainties on $\mathcal{M}/L$ are smaller (e.g., Dickinson et al. 2003). For the 34 DRGs in the FIRES fields, Förster–Schreiber et al. (2004) found median stellar masses of $\mathcal{M} = 0.8 - 1.6 \times 10^{11} \, \mathcal{M}_\odot$, with an interquartile range of $\sim 0.6 - 3 \times 10^{11} \, \mathcal{M}_\odot$ (using different assumptions for the star–formation history). Because our models are taken over a wider range of star–formation histories, we expect our stellar masses to be slightly lower with respect to those derived for constant star–formation models (Förster–Schreiber et al. 2004). Thus the range and average of the DRG stellar–mass distribution seem generally consistent with those in the FIRES fields (see also Labbé et al. 2005). The tail of lower–mass DRGs in our sample probably also arises from the greater number of objects with lower redshifts. Restricting our sample to a higher minimum redshift would further

increase the lower–bound of our interquartile range.

The long–dashed line in Figure 11 shows the stellar mass limit for a passively evolving stellar population formed in a single burst at $z = \infty$ and with $K_s = 23.2$ mag. Our DRG selection is approximately complete in stellar mass for passively evolving galaxies with $\mathcal{M} \geq 10^{11} \, \mathcal{M}_\odot$ to $2 \leq z \leq 3$, because no galaxy can have a mass–to–light ratio higher than a maximally old stellar population. Bluer galaxies with $\mathcal{M} \geq 10^{11} \, \mathcal{M}_\odot$ and lower mass–to–light ratios such as UV–luminous LBGs could be excluded by the $(J-K_s)_{\rm Vega} > 2.3$ mag selection. However, Shapley et al. (2005) infer that the majority of LBGs at $z \sim 2$ with $\mathcal{M} \geq 10^{11} \, \mathcal{M}_\odot$ would satisfy $(J-K_s)_{\rm Vega} > 2.3$ mag (see also, Reddy et al. 2005). At $z \leq 2$, the $J-K_s$ color selection may miss some passively evolving galaxies as the Balmer/4000 Å break shifts to wavelengths below the blue–edge of the J–band filter (Daddi et al. 2004). We consider the DRG selection roughly complete in stellar mass to $\mathcal{M} \geq 10^{11} \, \mathcal{M}_\odot$ over the majority of the redshift range $2 \leq z \leq 3$.

Based on the fits to the single–component models, the integrated DRG stellar mass density for objects at $2 \leq z \leq 3$ with $\mathcal{M} \geq 10^{11} \, \mathcal{M}_\odot$ is $2.4^{+0.5}_{-0.4} \times 10^7 \, \mathcal{M}_\odot \, {\rm Mpc}^{-3}$. This increases to $2.8^{+0.6}_{-0.5} \times 10^7 \, \mathcal{M}_\odot \, {\rm Mpc}^{-3}$ using the stellar masses derived from the two–component model fits. In both cases the uncertainties are estimated using a bootstrap resampling of the dataset, which constructs random samples of DRGs with the sample size taken from the Poisson, counting uncertainties, and stellar masses drawn from the measured distribution (with replacement) modulated by the inferred stellar–mass errors. However, many of the DRGs show evidence for an AGN, either based on X–ray detections, IR luminosity, or rest–frame near– and mid–IR colors (see § 6.3). These objects have relatively higher derived stellar masses (Figure 11), which could imply that AGN tend to reside in the most massive galaxies at these redshifts. Alternatively it could be that AGN may contribute to the rest–frame UV–to–near-IR emission, leading to unduly larger stellar mass estimates. To bound this effect, we recalculate the stellar mass densities excluding all DRGs with X–ray detections, $L_{\rm IR} \geq 10^{13} \, L_\odot$, or with AGN–like rest–frame near–IR colors. In this case, the stellar mass density decreases to $2.0^{+0.4}_{-0.4}$ and $2.4^{+0.4}_{-0.4} \times 10^7 \, \mathcal{M}_\odot \, {\rm Mpc}^{-3}$ for the single– and two–component models, respectively. In this case, the DRGs contribute 25–70% to the total stellar mass density integrated over all galaxies at $2 \leq z \leq 3$, in reasonable agreement with the conclusions of Rudnick et al. (2003) and Fontana et al. (2003).

6.1.4. *Star–Formation Rates and "Dead" Objects*

The 24 μm–detected DRGs span SFRs from $\sim 100 - 1000 \, \mathcal{M}_\odot \, {\rm yr}^{-1}$, excluding those objects directly detected in the *Chandra* data (see Figure 6). The mean SFR for these sources is $\simeq 500 \, \mathcal{M}_\odot \, {\rm yr}^{-1}$, with a systematic uncertainty in the 24 μm to SFR conversion of ≈ 0.5 dex. This value includes objects with $L_{\rm IR} \geq 10^{13} \, \mathcal{M}_\odot$ or rest–frame near–IR colors indicative of AGN (see § 6.3). Excluding these objects, the average SFR of the 24 μm–detected DRGs drops to $\simeq 400 \, \mathcal{M}_\odot \, {\rm yr}^{-1}$. The mean SFR for the complete DRG sample (including those not detected with MIPS at 24 μm) is lower still. Taking the conservative limit that the 24 μm– undetected DRGs have no ongoing star formation, the mean SFR is $\simeq 220 \, \mathcal{M}_\odot \, {\rm yr}^{-1}$ excluding the X–ray sources. This does not change if we also exclude those sources with infrared luminosities or colors indicative of AGN.
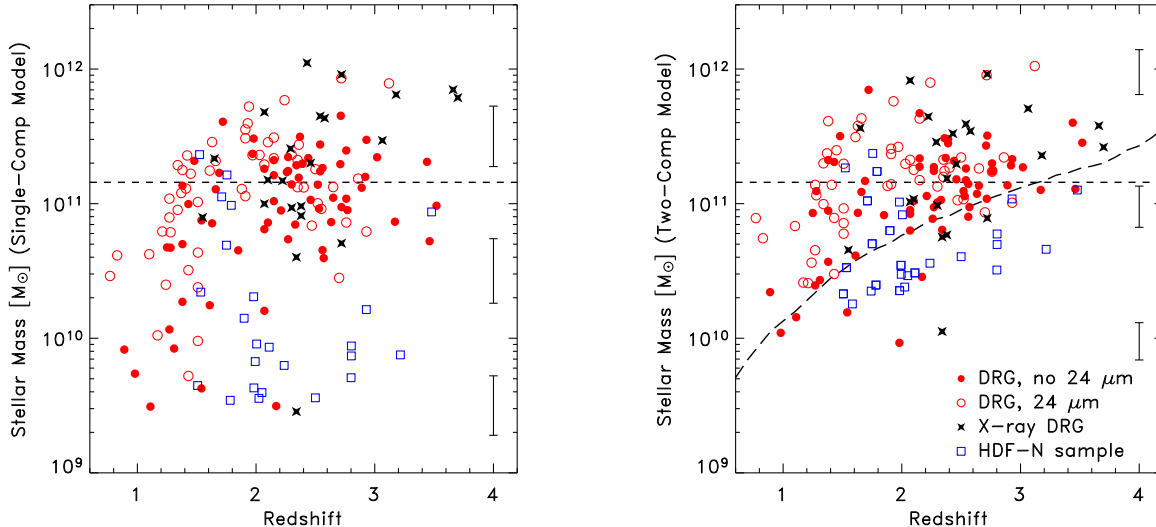
FIG. 11.— Stellar masses derived from modeling the galaxy SEDs, plotted as a function of redshift. The left panel shows the masses derived using the single–component, monotonically evolving star–formation histories. The right panel shows the masses derived using two–component models. In both panels filled red circles denote the GOODS–S DRGs undetected at 24 μm, and open red circles show those DRGs with 24 μm detections. Blue squares denote the galaxies in the HDF–N. Black stars show those DRGs with X–ray detections. Error bars are not shown for clarity, but mean error bars are shown as a function of galaxy stellar mass. The short–dashed line shows the value of the characteristic stellar mass of the present–day mass function (Cole et al. 2001). In the right panel, the long–dashed line shows the stellar–mass for a passively evolving stellar population formed instantaneously at $z = \infty$ with $K_s = 23.2$, which is the stellar–mass limit for the GOODS–S K_s–band data for such systems.

The mean SFR for the DRGs reported here is somewhat larger, but comparable to recent measurements of the "stacked" X–ray and sub–mm emission from DRG samples. Rubin et al. (2004) and Reddy et al. (2005) find the average SFR is $\sim 100-300$ $\mathcal{M}_\odot$ yr^{-1} based on statistical X–ray detections for DRGs with $K_s \lesssim 23$ AB mag. The inferred mean SFR for the various DRG populations is strongly dependent on the limiting K_s–band of the survey, and in the case of the X–ray derived measurements, on indications of AGN activity within the sample (see the discussion in Reddy et al. 2005). However, the X–ray SFR calibration has a systematic uncertainty on the order of a factor of five (Ranalli et al. 2003; Persic et al. 2004), owing to assumptions on the formation timescales of X–ray binaries in starbursts. A higher SFR–to–X–ray luminosity calibration may be appropriate for galaxies in the more intense starbursts such as those for the DRGs (Persic et al. 2004; Teng et al. 2005), so some scatter is expected in the conversion is expected. Knudsen et al. (2005) report an average SFR of 130 $\mathcal{M}_\odot$ yr^{-1}, based on a stacked sub–mm 850 μm flux density of DRGs with $K_s \leq 24.4$ AB mag, but is sensitive to the assumed average dust temperature (e.g., Chapman et al. 2005). Their sample extends to DRGs roughly a magnitude deeper in the K_s–band, and Reddy et al. (2005) demonstrate that the mean SFR of all types of star–forming galaxies at $z \sim 2$ (including DRGs) decreases with decreasing K_s–band flux density (see also Daddi et al. 2005b). Given the systematic uncertainties in the SFR calibrations, and the varying limiting magnitudes of the different DRG samples, we conclude that the mean SFR we derive using the MIPS 24 μm data for the GOODS–S DRGs is in broad agreement with these other values. The "typical" DRG is forming stars at rates in excess of $\gtrsim 200$ $\mathcal{M}_\odot$ yr^{-1}.

We can set an upper limit on the lifetime of a starburst in the DRGs at the gas–consumption timescale, defined to be the ratio of the gas mass to the SFR. For a massive galaxy with a molecular gas mass of $\mathcal{M}(H_2) \lesssim 10^{11}$ $\mathcal{M}_\odot$ (comparable to the gas reservoirs of the massive $z \gtrsim 3$ radio galaxies, De Breuck et al. 2003, 2005; Greve, Ivison, & Papadopoulos 2004), the gas–consumption timescale is $\lesssim 10^8 - 10^9$ yr for SFRs of $\sim 10^2 - 10^3$ $\mathcal{M}_\odot$ yr^{-1} (although these timescales would be shorter for lower gas masses, such as those in local ULIRGs, see Downes & Solomon 1998). This timescale is generally shorter than or comparable to the median ages we derive for the DRGs (consistent also with findings in Förster–Schreiber et al. 2004). Recent theoretical work suggests that high–redshift, massive galaxies quasi-continuously form stars at high rates for periods of 1–2 Gyr, with shorter periods ($\lesssim 100$ Myr) of boosted star formation (Nagamine et al. 2005; Finlator et al. 2005; De Lucia et al. 2005). If the DRGs sustain these the high SFRs for more than $\sim 10^8 - 10^9$ yr, then they will exhaust their gas supply unless fresh cold gas is repeatedly or continuously accreted. Kereš et al. (2005) predict that cold–gas accretion may dominate in massive galaxies at high redshifts, which may advocate such a scenario exists for the massive DRGs.

Assuming a lifetime of $\sim 10^8 - 10^9$ yr, a galaxy with a SFR of $10^2 - 10^3$ $\mathcal{M}_\odot$ yr^{-1} would assemble 10^{10-12} $\mathcal{M}_\odot$ in stars. If LBGs are forming stars rapidly and/or experiencing recurrent bursts at redshifts higher than that of the DRGs, $z \gtrsim 3.5$, then eventually they will assemble a sufficient population of late–type stars to dominate the optical to near–IR rest–frame light. It thus takes of order 1 Gyr to produce a DRG (unless high–redshift starbursts have an IMF weighted towards higher–mass stars, in which case even more time is required; Ferguson et al. 2002). Under these star–formation histories, the first progenitors of DRGs at z $\sim$ 2 to 3 should appear as starburst galaxies at z $\gtrsim$ 3 to 5. Massive star–forming galaxies appear to exist by $z \simeq 5$ from UV–dropout surveys (Eyles et al.
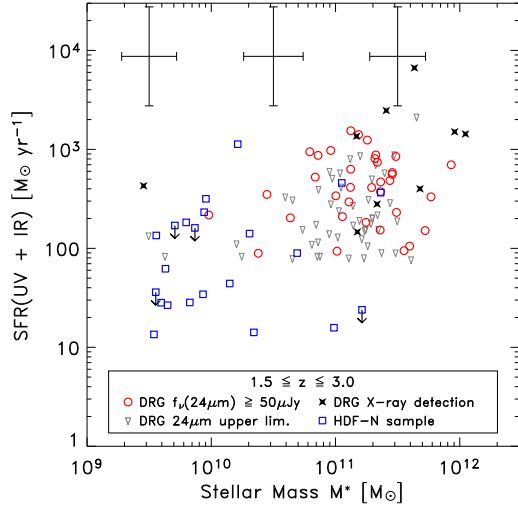
FIG. 12.— The SFRs derived from the sum of the UV and IR luminosities plotted as a function of galaxy stellar mass. Red circles denote the GOODS–S DRGs with 24 μm detections; gray triangles show upper limits for DRGs undetected at 24 μm, assuming they have $f_\nu(24\mu m) \leq 60$ μJy. Black stars indicate those DRGs with X–ray detections. Blue squares correspond to the 24 μm–selected galaxies in the HDF–N. All galaxy samples in this plot are restricted to the redshift range $1.5 \leq z \leq 3.0$. Systematics dominate the uncertainties on the SFRs and are ≈ 0.5 dex, as indicated by the inset error bars. The error bars also show the mean uncertainty on the stellar masses in three mass bins.

2005; Yan et al. 2005), and such objects could be forming the stellar populations that evolve to become the old components at the redshifts of the DRGs.

Based on the model fits, we find several candidates among the DRGs for passively evolving galaxies at high redshifts (see also § 3). There are 15 DRGs with best–fit models that favor older ages ($t \geq 1$ Gyr) that have undergone several e–folding times ($t/\tau \geq 3$) with low dust extinction ($E[B-V] \leq 0.1$) and no X–ray or 24 μm emission. Massive, "dead" DRGs are either galaxies that are between starbursts but already with a massive old stellar population, or galaxies that have completed the intense phase of their assembly. These galaxies span $1.9 \leq z \leq 3.0$, and have $i_{775} - K_s > 2.6$ and $K_s - [4.5\mu m] < 1.2$ (see also Figure 3 and discussion in § 3). These objects contribute $\simeq 4.9 \pm 1.4 \times 10^6$ $\mathcal{M}_\odot$ Mpc^{-3} to the global stellar mass density at these redshifts. Such massive, "dead" objects make up only a fairly low fraction of the stellar mass density ($\lesssim 10\%$) integrated over all galaxies at $z \sim 2-3$, and therefore are relatively rare at these redshifts. In contrast, early–type, massive ($\geq 10^{11}$ $\mathcal{M}_\odot$) galaxies account for $\sim 30\%$ of the total local stellar–mass density for the stellar–mass function of Bell et al. (2003, see also Baldry et al. 2004). Thus, the fraction of the global stellar–mass density in such galaxies increases threefold from $z \gtrsim 2$ to 0.

6.2. The Relation between Star Formation and Stellar Mass in Galaxies at $z \sim 1.5-3.0$

Figure 12 shows the SFRs as a function of the stellar mass for the DRGs and the HDF–N sample. The figure shows the stellar masses derived from the models with single–component star–formation histories, although using the two–component fits does not strongly change any of the conclusions. DRGs not detected at 24 μm by MIPS are shown as upper limits assuming that their 24 μm flux density is less

than the 50% completeness limit, $f_\nu(24\mu m) \leq 60$ μJy. We also restrict the DRG and HDF–N samples to those objects with $1.5 \leq z \leq 3.0$, where we are approximately complete for massive galaxies. Furthermore, restricting the sample to $z \leq 3$ removes few galaxies from the samples, and facilitates the contrast with the lower–redshift samples (see § 6.4).

The DRGs have higher stellar masses and SFRs relative to the HDF–N 24 μm–selected sample, owing primarily to the fainter flux limit of the 24 μm data in the HDF–N. There is a weak correlation between SFR and stellar mass, although this trend may be softened if the SFRs of DRGs with upper limits are in fact lower. Objects with stellar masses greater than 10^{11} $\mathcal{M}_\odot$ span 1.5 dex in SFR, excluding the X–ray–detected DRGs with inferred $L_{IR} \gtrsim 10^{13}$ $L_\odot$. The upper envelope of SFRs decreases for lower mass galaxies, and such objects should be detected in our data if present. Therefore, at these redshifts galaxies with the highest stellar masses also appear to be experiencing the highest SFRs.

6.3. Growth of Supermassive Black Holes in Massive, High–Redshift Galaxies

Many of the DRGs with the highest stellar masses and SFRs are detected in the deep X–ray data. Twelve of the 13 X–ray detected DRGs with $\mathcal{M}^* \geq 10^{11}$ $\mathcal{M}_\odot$ have X–ray to optical flux ratios, $\log f_X/f_R \geq -1.0$ (the remaining one has $\log f_X/f_R \sim -1.4$), and these imply the presence of an AGN with $L_X \gtrsim 10^{42}$ erg s^{-1} for DRGs at $z \gtrsim 1.5$ (e.g., Hornschemeier et al. 2001; Alexander et al. 2003). In addition, Worsley et al. (2005) conclude that as much as 40% of the hard X–ray background stems from heavily obscured AGN at $z \gtrsim 0.5$. Recent *Spitzer* IR observations are finding many AGN candidates whose X–ray, UV, and optical emission is heavily obscured by gas and dust, and missed in deep X–ray surveys (e.g., Alonso–Herrero et al. 2005; Donley et al. 2005). Alonso–Herrero et al. (2005) find that as many as 50% of MIPS 24 μm sources with red IRAC colors are not detected in the deep X–ray data. This suggests that AGN may be hidden behind sufficiently Compton–thick material that none of the direct X–ray emission escapes (Brandt & Hasinger 2005). Models of the X–ray background support this possibility (Gilli 2004).

At $1.5 \lesssim z \lesssim 3.5$, galaxies dominated by the light from stellar photospheres should have relatively blue $[4.5\mu m]-[8.0\mu m]$ colors (see § 3). Alternatively galaxies dominated by AGN emission in the rest–frame near–IR should have redder IRAC colors (see, e.g., Rieke 1978; Neugebauer et al. 1979; Lacy et al. 2004; Alonso–Herrero et al. 2005; Stern et al. 2005). Lacy et al. (2004) found that Seyfert 1 galaxies and obscured AGN have red $[4.5\mu m]-[8.0\mu m]$ colors, similar to the red rest–frame $J-K_s$ colors of Parkes Quasars in 2MASS at $z \sim 0-0.5$ (Francis et al. 2004). Similarly, of the non–X-ray detected DRGs with IRAC counterparts, roughly 25% (26/106) satisfy the IR color selection for AGN of Stern et al. (2005). Upon inspection of their individual SEDs, most are plausible AGN candidates with red IRAC colors. Four of these DRGs are star–forming objects at $z \gtrsim 2.9$ whose IRAC colors mimic those of AGN candidates at lower redshift. These galaxies are optically fainter and have higher redshifts than typical galaxies in the Stern et al. sample, and are an additional source of contamination in IR selection of AGN. An additional 10 of these DRGs have $z \simeq 1.0-1.4$ and their SEDs are consistent with heavily extincted starbursts whose $[8.0\mu m]$ magnitudes may be augmented by the 3 μm

PAH emission feature.[18] Excluding these 14 objects, approximately 10% (10/125) of the X-ray–undetected DRGs may have dust–enshrouded AGN that contribute some fraction of the rest–frame near– and mid–IR light. Combined with the 15% of X–ray–detected DRGs, perhaps a quarter of the DRG population host AGN, which implies they are actively growing their SMBHs.

The X-ray–detected fraction of DRGs apparently rises with increasing IR luminosity ($>50\%$ at $L_{IR} \gtrsim 10^{13} L_\odot$), a trend also seen in the analysis of X–ray emission from high–redshift sub–mm galaxies (Alexander et al. 2005). The GOODS–S field lacks deep sub–mm observations, which would allow us to explore any direct overlap between these coeval populations. Locally, the most luminous ULIRGs and HyLIRGs frequently host AGN sufficiently powerful to affect their global properties (Veilleux et al. 1995). If the IR–luminous DRGs are similar, then the high incidence of AGN is expected, especially for those with inferred $L_{IR} > 10^{13} L_\odot$. This implies that the massive galaxies at these epochs may be both assembling their stellar populations and growing SMBHs (see also L. Moustakas et al. in preparation). Locally, the space density of ULIRGs is $\approx 10^{-7} h_{70}$ Mpc^{-3} (Sanders et al. 2003), while the DRGs with ULIRG–like luminosities have a space density of $5.8 \pm 0.9 \times 10^{-5} h_{70}^{-3}$ Mpc^{-3} — an increase by a factor of 600 (and similar to the conclusion for *BzK*–selected objects, Daddi et al. 2005b). Thus, such objects are a much more common phenomenon at high redshift.

6.4. *Evolution of the Star Formation Rate as Function of Stellar Mass*

The DRGs have higher specific SFRs (SFR per unit stellar mass, $\Psi/\mathcal{M}$) than galaxies with comparable mass at lower redshifts ($z \lesssim 1$). Figure 13 shows the specific SFRs for DRGs and HDF–N galaxies at $1.5 \leq z \leq 3.0$, comparing them to galaxies at lower redshift in the COMBO–17 survey (see § 2.5). The SFRs for the COMBO–17 galaxies are calculated using the MIPS 24 μm imaging and rest–frame UV emission in an analogous manner as for the DRGs. Masses for COMBO–17 galaxies were estimated from their rest–frame $M(V)$ and $U - V$ colors, and have a typical uncertainty of 0.3 dex. This method will tend to *overestimate* the masses of galaxies involved in starbursts, but it is fairly robust for quiescent galaxies such as those that dominate our conclusions here (see Bell et al. 2004, 2005a).

We are biased against galaxies with low stellar masses and low specific SFRs, which causes the lower "envelope" in all the panels of Figure 13. This selection effect can produce the apparent anticorrelation between specific SFR and stellar mass (most apparent in the COMBO–17 galaxy plots). The galaxies at $z \lesssim 1$ show an upper envelope in the sense that there is a lack of galaxies with high specific SFRs and high stellar masses. In contrast, the DRGs at $1.5 \leq z \leq 3$ show a nearly unchanging range of specific SFRs at all stellar masses, although there is a hint that the DRGs at the high–mass end ($\mathcal{M} \geq 10^{11} \mathcal{M}_\odot$) show an upper envelope on their specific SFRs. Even then the massive galaxies have systematically higher specific SFRs than the $z \lesssim 1$ galaxies in COMBO–17. Quantitatively, the DRGs with $\mathcal{M} > 10^{11} \mathcal{M}_\odot$ and $1.5 \leq z \leq 3$ have specific SFRs of $\Psi/\mathcal{M} \sim 0.2 - 10$ Gyr^{-1}, with a mean

value of ~ 2.4 Gyr^{-1} (excluding those with X–ray detections). By $z \sim 0.7$ galaxies with $\mathcal{M} \geq 10^{11} \mathcal{M}_\odot$ have $\Psi/\mathcal{M} \sim 0.1 - 1$ Gyr^{-1} and at $z \sim 0.4$ galaxies with $\mathcal{M} \geq 10^{11} \mathcal{M}_\odot$ have $\Psi/\mathcal{M} \lesssim 0.5$ Gyr^{-1} — an order of magnitude lower than for the massive DRGs.

This downward evolution in the specific SFRs of massive galaxies has been referred to as "downsizing" (see § 1). The hypothesis is that massive galaxies host most of the SFR density at high redshifts, and that galaxy formation shifts to less–massive systems at lower redshifts. It is unclear if downsizing is a proper description as nearly *all* galaxies at $1.5 \lesssim z \lesssim 3.0$ have higher specific SFRs at higher redshift, not just the most massive. "Downsizing" is not equivalent to a global change in $\Psi/\mathcal{M}$ with redshift. However, our results indicate that star–formation in massive galaxies is reduced for $z \lesssim 1$ as galaxies with lower stellar masses have higher specific SFRs. It appears that massive galaxies are largely done assembling their stellar mass in high specific–SFR events by $z \sim 1.5$ (although mergers accompanied by low specific SFRs, i.e., "dry" mergers, could still take place at lower redshift, see, e.g., Bell et al. 2005b; Faber et al. 2005; van Dokkum 2005).

We define the integrated specific SFR, Υ, as the ratio of the sum of the SFRs, Ψ_i, to the sum of their stellar masses, $\mathcal{M}_i$, over all i galaxies,

$$\Upsilon = \frac{\sum_i \Psi_i}{\sum_i \mathcal{M}_i}. \tag{4}$$

This is essentially just the ratio of the SFR density to the stellar mass density for a volume–limited sample of galaxies. Figure 14 shows the integrated specific SFRs for DRGs at $1.5 \leq z \leq 3.0$ and COMBO–17 galaxies at $z \sim 0.4$ and 0.7 with $\mathcal{M} \geq 10^{11} \mathcal{M}_\odot$. The data point for the DRGs includes all DRGs with $\mathcal{M} \geq 10^{11} \mathcal{M}_\odot$, and assumes that the DRGs without 24 μm detections have a no star–formation ($\Psi = 0 \mathcal{M}_\odot$ yr^{-1}). The error box illustrates how changes in our assumptions affect the result. The bottom bound of the box shows the value if we exclude those objects with X–ray detections, or with IR luminosities or colors indicative of AGN (see § 6.3). The upper bound of the box shows the value for DRGs in this redshift and mass range, and if we calculate SFRs for the DRGs without 24 μm detections assuming they have $f_\nu(24\mu m) = 60 \mu$Jy. Note that for this calculation we have used the stellar masses from the single–component fits. Using those from the two–component fits increases the DRG point and error box by a small amount, <0.05 dex.

The integrated specific SFR in massive galaxies declines by more than an order of magnitude from $z \sim 1.5 - 3$ to redshifts $z \sim 0.7$ and 0.4. Using the rest–frame UV luminosities and [O II] emission–line fluxes of galaxies in the Gemini Deep–Deep Survey, Juneau et al. (2005) found that the specific SFRs of galaxies with $\mathcal{M} \geq 10^{10.8} \mathcal{M}_\odot$ decline by roughly a factor of six from $z \sim 2$ to 1. Our results suggest that this value may be underestimated when the IR emission from these galaxies is included in the SFR determination.

Figure 14 shows the specific SFR integrated over all galaxies by taking the ratio of the cosmic SFR density to the integrated SFR density from Cole et al. (2001), i.e., $\Upsilon = \dot{\rho}_* / \int \dot{\rho}_* dt$ and also from the predictions from Hernquist & Springel (2003). The integrated specific SFR over all galaxies declines steadily with decreasing redshift, because the SFR density peaks between $z \sim 1 - 3$ (Hopkins 2004), corresponding to when the stellar mass density appears to have grown the most rapidly (Dickinson et al. 2003). That is, there is a decrease in the global specific SFR.

---

[18] Stern et al. (2005) find that 17% of objects satisfying their IRAC color–color selection are spectroscopically classified as galaxies, roughly consistent with the galaxy contamination here, modulo differences in survey limiting magnitudes.
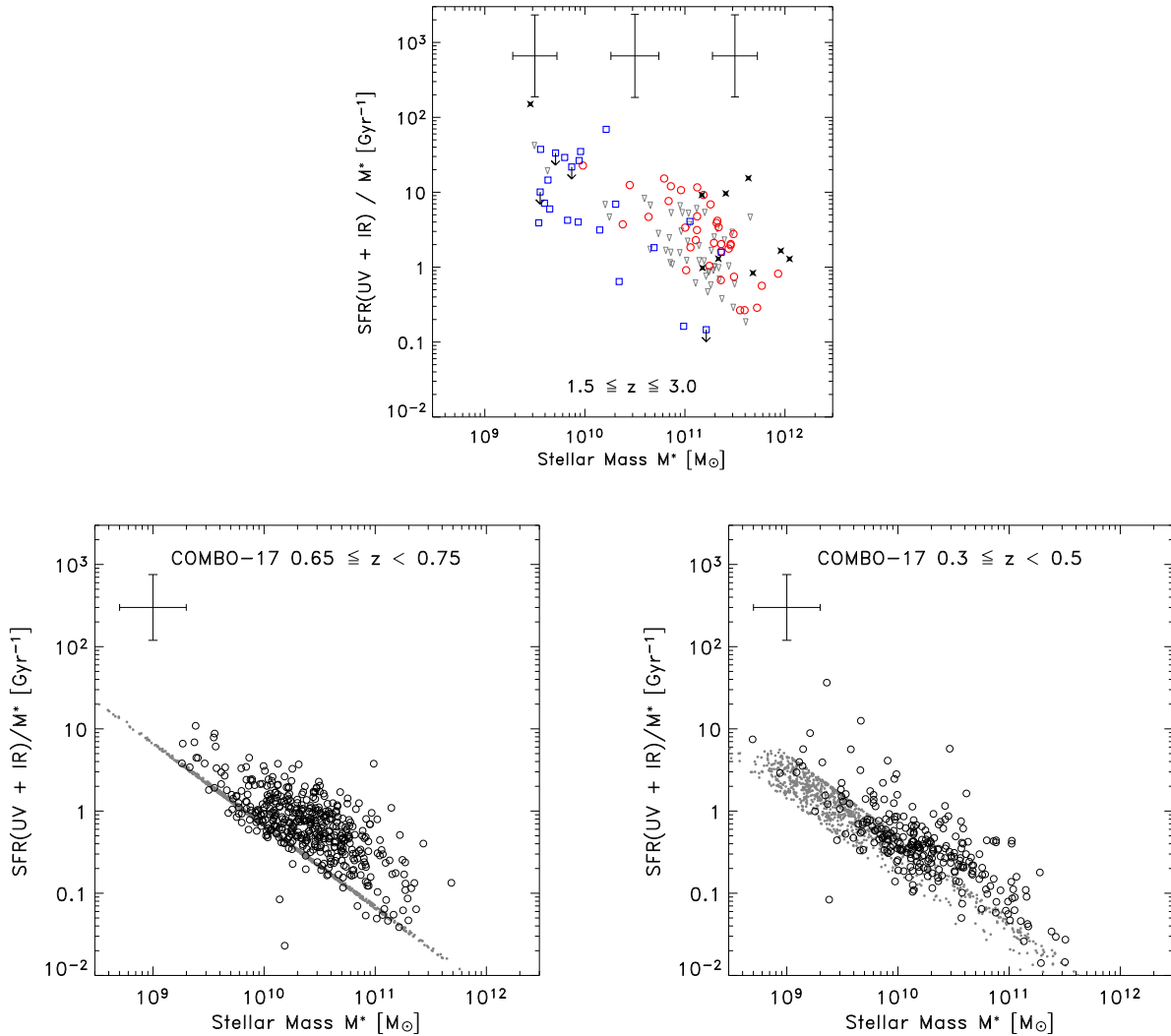
FIG. 13.— The specific SFR as a function of galaxy stellar mass. The top panel shows the results for the DRG sample and the HDF–N galaxies, all restricted to $1.5 \leq z \leq 3.0$, with symbols and errors as in Figure 12. The bottom panels show the specific SFRs as a function of stellar mass for lower–redshift galaxy samples from the COMBO–17 survey (as labeled). Open circles show COMBO–17 galaxies detected with *Spitzer* at 24 μm, and small filled circles show upper limits for COMBO–17 galaxies undetected at 24 μm.

The evolution in the integrated specific SFR in massive galaxies is accelerated relative to the integrated global value for all galaxies. Galaxies with $\mathcal{M} \geq 10^{11}\, \mathcal{M}_\odot$ at $z \sim 1.5-3$ were forming stars at or slightly above the rate integrated over all galaxies. These massive galaxies contribute between 10–30% to the global SFR density at $z \sim 1.5-3$ (comparing to Hopkins 2004). In contrast, by $z \lesssim 1$, galaxies with $\mathcal{M} \geq 10^{11}\, \mathcal{M}_\odot$ have an integrated specific SFR much lower than value integrated over all galaxies. Thus, our results indicate that by $z \lesssim 1$ massive galaxies have formed most of their stellar mass, and lower–mass galaxies dominate the cosmic SFR density. If we tried to track individual galaxies we would need to account for their growth in mass from $z \sim 3$ to $z \lesssim 1$, and as a result this trend would be even stronger.

Our conclusion would be undermined if there were a substantial population of passively evolving, massive galaxies at high redshifts that we have missed in our selection. The GOODS–S DRG sample is approximately mass–limited for passively evolving galaxies to $10^{11}\, \mathcal{M}_\odot$ at $2 \leq z \leq 3$, al-

though we are presumably missing some at $z \leq 2$ (see Daddi et al. 2004, and § 6.1.3). However, if we restrict the calculation to those DRGs with $2 \leq z \leq 3$, the integrated specific SFR *increases* by roughly 0.1 dex. Including those sources at $z < 2$ provides a more conservative measure of the evolution in the specific SFRs of massive galaxies, so we keep these objects here. The DRG selection is potentially biased against other star–forming galaxies, most notably UV–luminous LBGs. However, LBGs with these stellar masses have high inferred SFRs, comparable even to those of the DRGs (see, e.g., Shapley et al. 2003; and Figure 5). Moreover, Shapley et al. find that the inferred $J-K_s$ colors of most UV–selected LBGs at $z \sim 2$ with $\mathcal{M} \geq 10^{11}\, \mathcal{M}_\odot$ satisfy the DRG selection criterion. Therefore, including massive LBGs into the integrated specific SFR would have little effect on our conclusions, and we are confident that the results presented here apply to the general galaxy population at $z \sim 1.5-3$ with $\mathcal{M} \geq 10^{11}\, \mathcal{M}_\odot$.

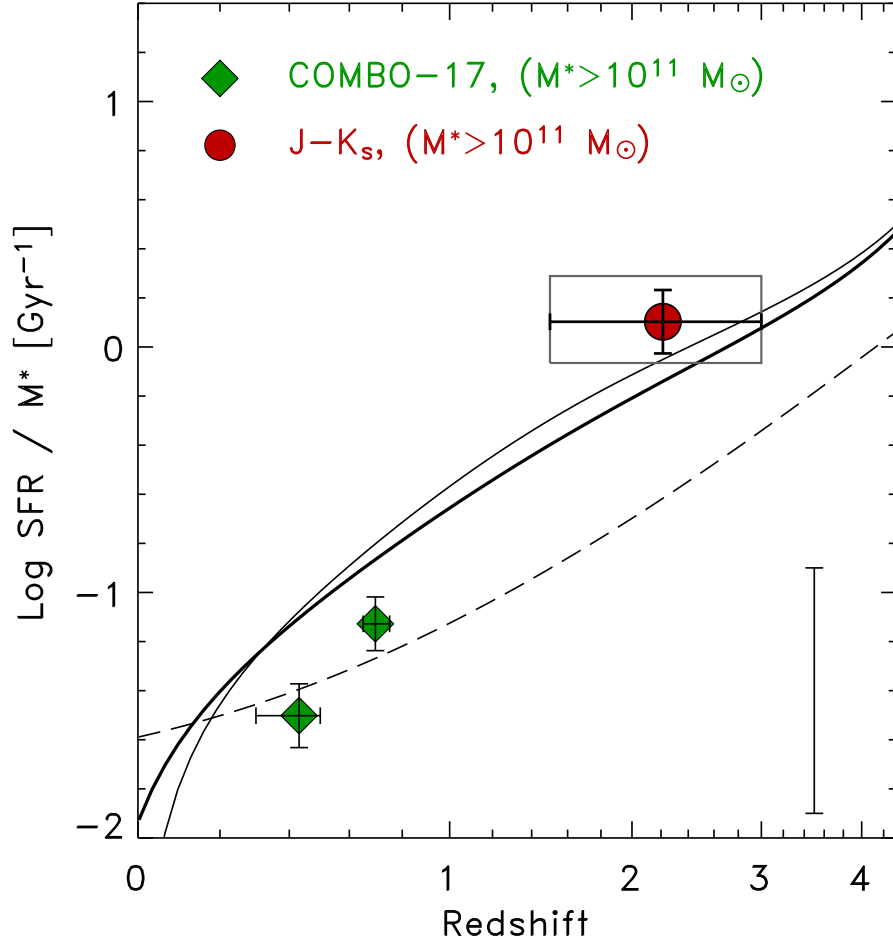This decline in the specific SFR of massive galaxies seems

FIG. 14.— Evolution of the integrated specific SFR, i.e., the ratio of the total SFR to the total stellar mass. The curves show the expected evolution of the ratio of the total SFR to the total galaxy stellar mass densities from an empirical fit to the evolution of the SFR density (solid lines, thick line includes correction for dust extinction; Cole et al. 2001), and the model of Hernquist & Springel (dashed line; 2003). The data points show results for galaxies with $\mathcal{M} \geq 10^{11} \mathcal{M}_\odot$. The filled diamonds show the mean values derived for COMBO–17 galaxies, and the filled circle shows the mean value for the DRGs. The data point for the DRGs sets the SFR of those galaxies without MIPS detections to zero. The lower bound of the box around the DRG point shows the value if we exclude those DRGs with direct X–ray detections, and those DRGs with $L_{IR} \geq 10^{13} L_\odot$ or IR colors indicative of AGN (see text). The upper bound shows the value for the DRGs with no MIPS detection have $f_\nu(24\mu m) = 60 \mu Jy$. The error bars on the data points themselves are derived by a bootstrap resampling of the dataset. These do not include systematic uncertainties in the SFRs, which are indicated by the inset error bar.

to signify the point where massive galaxies have formed the bulk of their stellar populations. This may happen because they have converted most of their gas reservoirs into stellar mass, and thus can no longer sustain high SFRs. This may be supported by the timescales for the galaxies to sustain their current SFRs discussed in § 6.1.4. Alternatively, because some of the massive DRGs show indications that they are fueling powerful AGN, it may be that AGN feedback provides a means to suppress further star formation in these objects (Hopkins et al. 2005). To understand the rapid evolution in the specific SFRs of massive galaxies at these redshifts, we will need to better understand the coeval assembly of stellar mass and AGN, and the energetic feedback from the processes.

7. CONCLUSIONS

We have investigated the properties of massive, star–forming galaxies at $z \sim 1 - 3.5$ using observations from the

Hubble Space Telescope, ground–based near–infrared (IR) imaging, and IR observations from the *Spitzer Space Telescope* at 3–24 μm. From a K_s–selected galaxy sample over a $\simeq 130$ arcmin^2 field in GOODS–S, we identified 153 DRGs with $(J-K_s)_{Vega} \geq 2.3$ to $K_s \leq 23.2$ mag, which is approximately complete in stellar mass to $10^{11} \mathcal{M}_\odot$ for $z \leq 3$. The majority of DRGs (90%) are detected in deep *Spitzer*/IRAC imaging at $3.6 - 8.0$ μm, and the remainder are confused with nearby sources within the IRAC beam. Roughly half of the DRGs are detected by *Spitzer*/MIPS at 24 μm with $f_\nu(24\mu m) \geq 50$ μJy. At $z \sim 1 - 3.5$, these 24 μm flux densities correspond to IR luminosities of $L_{IR} \sim 10^{11-13} L_\odot$.

Based on the full suite of photometry, we find that the DRG selection identifies galaxies whose optical rest–frame light is dominated by a population of evolved stars combined with trace amounts of ongoing star formation ($z_{med} \sim 2.5$), and galaxies whose light is dominated by heavily extinced ($A_{1600} \gtrsim 4 - 6$ mag) starbursts ($z_{med} \sim 1.7$), in roughly equal

proportions. Only a very small fraction of the DRGs ($\lesssim 10\%$) in the sample have SEDs consistent with pure old ($\gtrsim 1$ Gyr) stellar populations with no indication of current star formation. We estimate that the number density of massive, passively evolving DRGs at $2 \leq z \leq 3$ is $3.2 \times 10^{-5}\ h_{70}^{-3}$ Mpc^{-3}, which is nearly an order of magnitude lower than that for DRGs in the HDF–S (Labbé et al. 2005), although some of this discrepancy likely results from the fact that the HDF–S sample extends to fainter K_s–band sources. The candidates for passively–evolving DRGs at $2 \leq z \leq 3$ with $\mathcal{M} \geq 10^{11}\ \mathcal{M}_\odot$ contribute only a small fraction ($\lesssim 10\%$) to the global stellar–mass density integrated over all galaxies at these redshifts. Thus, massive, passively evolving objects are rare at $z \gtrsim 2$. However, the fraction of the stellar–mass density in massive, passively evolving galaxies increases threefold from $z \gtrsim 2$ to 0.

The UV–derived SFRs for the DRGs are lower than those that include the reradiated IR emission by up to two orders of magnitude. The DRGs have IR/UV luminosity ratios typically in excess of what is expected from their rest–frame UV spectral slope, consistent with observations of local LIRGs and ULIRGs.

We compare the DRG photometry to stellar population synthesis models to estimate the stellar masses and to study the properties of the stars that dominate the rest–frame UV through near–IR light. Models allowing for a previous stellar population formed in an instantaneous burst in the distant past accompanied by additional on–going star–formation generally provide better fits to the data. We conclude that the DRGs have complex and stochastic star–formation histories consistent with other star–forming galaxies at these redshifts and locally, and with predictions from hierarchical models.

DRGs at $z \sim 1.5 - 3$ with stellar masses greater than $10^{11}\ \mathcal{M}_\odot$ have specific SFRs ranging from $0.2 - 10$ Gyr^{-1}. This is more than an order of magnitude larger than that derived for galaxies with stellar masses above $10^{11}\ \mathcal{M}_\odot$ at $z \sim 0.7$ and 0.4. Simultaneously, the most luminous and massive DRGs show indications for the presence of AGN either based on X–ray luminosity, IR luminosities, or IR colors. We find that as many as one–quarter of the DRG population contain AGN, and therefore the growth of SMBHs coincides with the formation of massive galaxies at $z \gtrsim 1.5$. Further implications from the prevalence of AGN in DRGs will be discussed in L. Moustakas et al. (in preparation).

At $z \gtrsim 1.5$, galaxies with stellar masses $> 10^{11}\ \mathcal{M}_\odot$ are forming stars at rates at or slightly higher than the global value integrated over all galaxies at this epoch. In contrast, galaxies at $z \lesssim 0.7$ with $\mathcal{M} \geq 10^{11}\ \mathcal{M}_\odot$ are forming stars at rates less than the global value for all galaxies. The evolution in the specific SFRs of massive galaxies occurs at an accelerated rate compared to that of all galaxies. The bulk of star formation in massive galaxies occurs at early cosmic epochs and that further mass assembly in these galaxies is accompanied by low specific SFRs. At $z \lesssim 1$ massive galaxies have formed most of their stellar mass, and lower mass galaxies dominate the cosmic SFR density.

REFERENCES

Adelberger, K. L., & Steidel, C. C. 2000, ApJ, 544, 218
Alexander, D. M., et al. 2003, AJ, 126, 539
Alexander, D. M., Smail, I., Bauer, F. E., Chapman, S. C., Blain, A. W., Brandt, W. N., & Ivison, R. J. 2005, Nature, 434, 738
Alonso–Herrero, A., et al., 2005, ApJ, submitted
Appleton, P. N., et al. 2004, ApJS, 154, 147
Baldry, I. K., & Glazebrook, K. 2003, ApJ, 593, 258
Baldry, I. K., Glazebrook, K., Brinkmann, J., Ivezić, Ž., Lupton, R. H., Nichol, R. C., & Szalay, A. S. 2004, ApJ, 600, 681
Barger, A. J., Cowie, L. L., & Richards, E. A. 2000, AJ, 119, 2092
Bauer, A. E., Drory, N., Hill, G. J., & Feulner, G. 2005, ApJ, 621, L89
Baugh, C. M., Cole, S., Frenk, C. S., & Lacey, C. G. 1998, ApJ, 498, 504
Baugh, C. M., Lacey, C. G., Frenk, C. S., Granato, G. L., Silva, L., Bressan, A., Benson, A. J., & Cole, S. 2005, MNRAS, 356, 1191
Bell, E. F. 2003, ApJ, 586, 794
Bell, E. F., McIntosh, D. H., Katz, N., & Weinberg, M. D. 2003, ApJS, 149, 289
Bell, E. F., et al. 2004, ApJ, 608, 752
Bell, E. F., et al. 2005a, ApJ, 625, 23
Bell, E. F., et al. 2005b, ApJ, submitted (astro–ph/0506425)
Bertin, E., & Arnouts, S. 1996, A&AS, 117, 393
Blain, A. W., Smail, I., Ivison, R. J., Kneib, J.-P., & Frayer, D. T. 2002, Phys. Rep., 369, 111
Blain, A. W., Chapman, S. C., Smail, I., & Ivison, R. 2004, ApJ, 611, 725
Bouwens, R. J., et al. 2004, ApJ, 606, L25
Brandt, W. N., & Hasinger, G. 2005, ARA&A, in press (astro–ph/0501058)
Brinchmann, J., & Ellis, R. S. 2000, ApJ, 536, L77
Bruzual, G. A., & Charlot, S. 2003, MNRAS, 344, 1000
Budavári, T., Szalay, A. S., Connolly, A. J., Csabai, I., & Dickinson, M. 2000, AJ, 120, 1588
Buat, V., et al. 2005, ApJ, 619, L51
Calzetti, D., Armus, L., Bohlin, R. C., Kinney, A. L., Koornneef, J., & Storchi-Bergmann, T. 2000, ApJ, 533, 682
Calzetti, D., Kinney, A. L., & Storchi-Bergmann, T. 1994, ApJ, 429, 582
Caputi, K., et al. 2005, ApJ, submitted
Chary, R. R., & Elbaz, D. 2001, ApJ, 556, 562
Chapman, S. C., Helou, G., Lewis, G. F., & Dale, D. A. 2003, ApJ, 588, 186
Chapman, S. C., Blain, A. W., Smail, I., & Ivison, R. J. 2005, ApJ, 622, 772
Charmandaris, V., Le Floc'h, E., & Mirabel, I. F. 2004, ApJ, 600, L15
Cimatti, A., et al. 2002a, A&A, 381, L68
Cimatti, A., et al. 2002b, A&A, 391, L1
Cole, S., et al. 2001, MNRAS, 326, 255
Coleman, G. D., Wu, C.-C., & Weedman, D. W. 1980, ApJS, 43, 393
Cowie, L. L., Songaila, A., & Barger, A. J. 1999, AJ, 118, 603
Daddi, E., et al. 2003, ApJ, 588, 50
Daddi, E., Cimatti, A., Renzini, A., Fontana, A., Mignoli, M., Pozzetti, L., Tozzi, P., & Zamorani, G. 2004, ApJ, 617, 746
Daddi, E., et al. 2005a, ApJ, 626, 680

Daddi, E., et al. 2005b, ApJ, 631, L13
Dale, D. A., Helou, G., Contursi, A., Silbermann, N. A., & Kolhatkar, S., 2001, ApJ, 549, 215
Dale, D. A., & Helou, G. 2002, ApJ, 576, 159
De Breuck, C., et al. 2003, A&A, 401, 911
De Breuck, C., Downes, D., Neri, R., van Breugel, W., Reuland, M., Omont, A., & Ivison, R. 2005, A&A, 430, L1
De Lucia, G., Springel, V., White, S. D. M., Croton, D., & Kauffmann, G. K. 2005, MNRAS, submitted (astro-ph/0509725)
Di Matteo, T., Springel, V., & Hernquist, L. 2005, Nature, 433, 604
Dickinson, M. et al. 2000, ApJ, 531, 624
Dickinson, M., Papovich, C., Ferguson, H. C., & Budavári, T. 2003, ApJ, 587, 25
Donley, J. L., Rieke, G. H., Rigby, J., & Pérez–González, P. G. 2005, ApJ, in press (astro-ph/0507676)
Downes, D., & Solomon, P. M. 1998, ApJ, 507, 615
Dunlop, J., Peacock, J., Spinrad, H., Dey, A., Jimenez, R., Stern, D., & Windhorst, R. A. 1996, Nature, 381, 581
Eggen, O. J., Lynden–Bel, D., & Sandage, A. R., 1962, ApJ, 136, 748
Elbaz, D., Cesarsky, C. J., Chanial, P., Aussel, H., Franceschini, A., Fadda, D., & Chary, R. R. 2002, A&A, 384, 848
Eyles, L., Bunker A., Stanway, E., Lacy, M., & Ellis, R. 2005, MNRAS, in press (astro–ph/0502385)
Faber, S. M., et al. 2005, ApJ, submitted (astro–ph/0506044)
Ferguson, H. C., Dickinson, M., & Papovich, C. 2002, ApJ, 569, L65
Finlator, K., Davé, R., Papovich, C., & Hernquist, L. 2005, ApJ, submitted (astro–ph/0507719)
Fontana, A., et al. 2003, ApJ, 594, L9
Fontana, A., et al. 2004, A&A, 424, 23
Förster–Schreiber, N. M., Genzel, R., Lutz, D., & Sternberg, A. 2003, ApJ, 599, 193
Förster–Schreiber, N. M. et al., 2004, ApJ, 616, 40
Francis, P. J., Nelson, B. O., & Cutri, R. M. 2004, AJ, 127, 646
Franx, M., et al. 2003, ApJ, 587, L79
Gebhardt, K., et al. 2000, ApJ, 539, L13
Giacconi, R., et al. 2002, ApJS, 139, 369
Giavalisco, M. 2002, ARA&A, 40, 579
Giavalisco, M., et al. 2004a, ApJ, 600, L93
Giavalisco, M., et al. 2004b, ApJ, 600, L103
Gilli, R. 2004, Adv. Space Res., 34, 2470
Glazebrook, K., et al. 2004, Nature, 430, 181
Goldader, J. D., Meurer, G., Heckman, T. M., Seibert, M., Sanders, D. B., Calzetti, D., & Steidel, C. C. 2002, ApJ, 568, 651
Gordon, K., et al. 2005, PASP, 117, 503
Granato, G. L., Silva, L., Monaco, P., Panuzzo, P., Salucci, P., De Zotti, G., & Danese, L. 2001, MNRAS, 324, 757
Greve, T. R., Ivison, R. J., Papadopoulos, P. P. 2004, A&A, 419, 99
Haas, M., et al. 2003, A&A, 402, 87
Heavens, A., Panter, B., Jimenez, R., & Dunlop, J. 2004, Nature, 428, 625
Hernquist, L., & Springel, V. 2003, MNRAS, 341, 1253
Hopkins, A. 2004, ApJ, 615, 209
Hopkins, P. F., Hernquist, L., Cox, T. J., Di Matteo, T., Martini, P., Robertson, B., & Springel, V. 2005, ApJ, 625, 71
Hornschemeier, A., et al. 2001, ApJ, 554, 742
Im, M., Yamada, T., Tanaka, I., & Kajisawa, M. 2002, ApJ, 578, L19
Juneau, S., et al. 2005, ApJ, 619, L135
Kauffmann, G., & Charlot, S. 1998, MNRAS, 294, 705
Kauffmann, G., White, S. D. M., Heckman, T. M., Ménard, B., Brinchmann, J., Charlot, S., Tremonti, C., & Brinkmann, J. 2004, MNRAS, 353, 713
Kennicutt, R. C. 1998, ARA&A, 36, 189
Kereš, D., Katz, N., Weinberg, D. H., & Davé, R. 2005, MNRAS, 823
Kinney, A. L., Calzetti, D., Bohlin, R. C., McQuade, K., Storchi-Bergmann, T., & Schmitt, H. R. 1996, ApJ, 467, 38
Knudsen, K. K., et al. 2005, ApJ, in press (astro–ph/0509104)
Kong, X., Charlot, S., Brinchmann, J., & Fall, S. M. 2004, MNRAS, 349, 769
Labbé, I. et al. 2005, ApJ, 624, L81
Lacy, M., et al. 2004, ApJS, 154, 166
Larson, R. B. 2005, MNRAS, 359, 211
Le Fèvre, O., et al. 2004, A&A, 428, 1043
Le Floc'h, E., Mirabel, I. F., Laurent, O., Charmandaris, V., Gallais, P., Sauvage, M., Vigroux, L., & Cesarsky, C. 2001, A&A, 367, 487
Le Floc'h, E., et al. 2005, ApJ, in press (astro–ph/0506462)
Madau, P., Pozzetti, L., & Dickinson, M. 1998, ApJ, 498, 106
Magorrian, J., et al. 1998, AJ, 115, 2285
Marcillac, D., Elbaz, D., Chary, R. R., Dickinson, M., Galliano, F., & Morrison, G. 2005, A&A, submitted
McCarthy, P. J. 2004, ARA&A, 42, 477
McCarthy, P. J., et al. 2004, ApJ, 614, L9

Meurer, G., Heckman, T. M., & Calzetti, D. 1999, ApJ, 521, 64
Mignoli, M., et al. 2005, A&A, 437, 883
Mobasher, B., et al. 2004, ApJ, 600, L167
Moustakas, L. A., & Somerville, R. S. 2002, ApJ, 577, 1
Moustakas, L. A., et al. 2004, ApJ, 600, L131
Nagamine, K., Cen, R., Hernquist, L, Ostriker, J. P., & Springel, V. 2005, ApJ, 627, 608
Neugebauer, G., Oke, J. B., Becklin, E. G., & Matthews, K. 1979, ApJ230, 79
Papovich, C., Dickinson, M., & Ferguson, H. C. 2001, ApJ, 559, 620
Papovich, C., & Bell, E. F. 2002, ApJ, 579, L1
Papovich, C., et al. 2004a, ApJ, 600, L111
Papovich, C., et al. 2004b, ApJS, 154, 70
Papovich, C., Dickinson, M., Giavalisco, M., Conselice, C. J., & Ferguson, H. C. 2005, ApJ, 631, 101
Pérez–González, P. G. et al. 2005, ApJ, 630, 82
Persic, M., Rephaeli, Y., Braito, V., Cappi, M., Della Ceca, R., Franceschini, A., & Gruber, D. E. 2004, A&A, 419, 849
Ranalli, P., Comastri, A., & Setti, G. 2003, A&A, 399, 39
Reddy, N. A., Erb, D. K., Steidel, C. C., Shapley, A. E., Adelberger, K. L., & Pettini, M. 2005, ApJ, in press (astro-ph/0507264)
Rieke, G. H. 1978, ApJ, 226, 550
Roussel, H., Sauvage, M., Vigroux, L., & Bosma, A. 2001, A&A, 372, 427
Rubin, K. H. R., van Dokkum, P. G., Coppi, P., Johnson, O., Förster Schreiber, N. M., Franx, M., & van der Werf, P. 2004, ApJ, 613, L5
Rudnick, G., et al. 2003, ApJ, 599, 847
Sanders, D. B., Soifer, B. T., Elias, J. H., Neugebauer, G., & Matthews, K. 1988, ApJ, 328, L35
Sanders, D. B., & Mirabel, I. F. 1996, ARA&A, 34, 749
Sanders, D. B., Mazzarella, J. M., Kim, D.-C., Surace, J. A., & Soifer, B. T. 2003, AJ, 126, 1607
Sawicki, M. & Yee, H. K. C. 1998, AJ, 115, 1329
Sawicki, M. 2002, AJ, 124, 3050
Shapley, A. E., Steidel, C. C., Adelberger, K. L., Dickinson, M., Giavalisco, M., & Pettini, M. 2001, ApJ, 562, 95
Shapley, A. E., Erb, D. K., Pettini, M., Steidel, C. C., & Adelberger, K. L. 2004, ApJ, 612, 108
Shapley, A. E., Steidel, C. C., Erb, D. K., Reddy, N. A., Adelberger, K. L., Pettini, M., Barmby, P., & Huang, J. 2005, ApJ, 626, 698
Simpson, C., & Eisenhardt, P. 1999, PASP, 111, 691
Silva, L., Granato, G. L., Bressan, A., & Danese, L. 1998, ApJ, 509, 103
Smail, I., Owen, F. N., Morrison, G. E., Keel, W. C., Ivison, R. J., & Ledlow, M. J. 2002, ApJ, 581, 844
Soifer, B. T., Cohen, J. G., Armus, L., Matthews, K., Neugebauer, G., & Oke, J. B. 1995, ApJ, 443, L65
Somerville, R. S., Primack, J. R., & Faber, S. M. 2001, MNRAS, 320, 504
Spinoglio, L., Malkan, M. A., Rush, B., Carrasco, L., & Recillas-Cruz, E. 1995, ApJ, 453, 616
Spinrad, H., Dey, A., Stern, D., Dunlop, J., Peacock, J., Jimenez, R., & Windhorst, R. 1997, ApJ, 484, 581
Spoon, H. W. W., Moorwood, A. F. M., Lutz, D., Tielens, A. G. G. M., Siebenmorgen, R., & Keane, J. V. 2004, A&A, 414, 873
Springel, V., Di Matteo, T., & Hernquist, L. 2005a, ApJ, 620, L79
Springel, V., et al. 2005b, Nature, 435, 629
Steidel, C. C., Giavalisco, M., Pettini, M., Dickinson, M., & Adelberger, K. L. 1996, ApJ, 462, L17
Steidel, C. C., Adelberger, K. L., Giavalisco, M., Dickinson, M., & Pettini, M. 1999, ApJ, 519, 1
Stern, D., et al. 2005, ApJ, 631, 163
Szokoly, G. P., et al. 2004, ApJS, 155, 271
Teng, S. H., Wilson, A. S., Veilleux, S., Young, A. J., Sanders, D. B., & Nagar, N. M. 2005, ApJ, in press (astro–ph/0508112)
Totani, T., Yoshii, Y., Iwamuro, F., Maihara, T., & Motohara, K. 2001, ApJ, 558, L87
Treu, T., Ellis, R. S., Liao, T. X., & van Dokkum, P. G. 2005, ApJ, 622, L5
van Dokkum, P. G., et al. 2003, ApJ, 587, L83
van Dokkum, P. G., et al. 2004, ApJ, 611, 703
van Dokkum, P. G. 2005, ApJ, submitted (astro-ph/0506661)
van Dokkum, P. G., Kriek, M., Rodgers, B., Franx, M., & Puxley, P. 2005, ApJ, 622, L33
Vanzella, E., et al. 2005, A&A, 434, 53
Veilleux, S., Kim, D.-C., Sanders, D. B., Mazzarella, J. M., & Soifer, B. T. 1995, ApJS, 98, 171
Veilleux, S., Kim, D.-C., & Sanders, D. B. 1999, ApJ, 522, 113
Williams, R. E., et al. 1996, AJ, 112, 1335
Wilson, G., et al. 2004, ApJS, 154, 107
Wolf, C., Meisenheimer, K., Rix, H.–W. Borch, A., Dye, S., & Kleinheinrich, M. 2003, A&A, 401, 73

Wolf, C., et al. 2004, A&A, 421, 913
Worsley, M. A., et al. 2005, MNRAS, 357, 1281
Yan, H., et al. 2004a, ApJ, 616, 63
Yan, H., et al. 2005, ApJ, in press (astro-ph/0507673)

Yan, L., et al. 2004b, ApJS, 154, 75